Lisa Radl, BSc

# Fabrication of Copper Oxide Thin Films by Spray Pyrolysis Technique for CMOS Integrated Conductometric Gas Sensors

**MASTERARBEIT**

zur Erlangung des akademischen Grades

Diplom-Ingenieurin

Masterstudium Technische Chemie

eingereicht an der

**Technischen Universität Graz**

Betreuer

Univ.-Doz. Mag. Dr. Anton Köck

Materials Center Leoben Forschung GmbH

Materialien für Mikroelektronik

Graz, September 2019

## EIDESSTATTLICHE ERKLÄRUNG

Ich erkläre an Eides statt, dass ich die vorliegende Arbeit selbstständig verfasst, andere als die angegebenen Quellen/Hilfsmittel nicht benutzt, und die den benutzten Quellen wörtlich und inhaltlich entnommenen Stellen als solche kenntlich gemacht habe. Das in TUGRAZonline hochgeladene Textdokument ist mit der vorliegenden Masterarbeit identisch.

Datum

Unterschrift

# Abstract (English)

Gas sensors are widely used in a great variety of application fields ranging from air quality monitoring of buildings (smart home) to environmental monitoring by smartphones and to early disease-specific diagnosis by breath analysis (smart health). For these applications, gas sensors need a high sensitivity and especially a high selectivity to be able to detect a specific gas in a gas mixture. Currently, semiconducting metal oxide gas sensors constitute one of the most investigated groups of gas sensors in these application fields. Their detection principle relies on conductivity changes of the gas sensitive material due to adsorption and desorption processes on the solid – gas interface. Compared to well established n-type metal oxide semiconductor gas sensors, little is known about those based on p-type metal oxides as gas sensitive material.

Within this work, a p-type metal oxide material, namely copper (II) oxide, is deposited as thin film on silicon wafers. The copper (II) oxide thin films are deposited by copper nitrate, copper chloride or copper acetate precursor solutions varying between 0.05 – 0.3 M via spray pyrolysis technology. For deposition of the thin films not only precursor solutions and their concentration, but also spray time, deposition temperature and the distance between nozzle and substrate are essential processing parameters and are varied to optimize the spray pyrolysis process. The films are fully characterized by x-ray diffraction, Raman spectroscopy, optical light microscopy, scanning electron microscopy and atomic force microscopy. In a subsequent processing step, those thin films are structured by means of photolithography and are finally assembled to gas sensors. The gas sensing properties of the fabricated sensors are investigated upon exposure to $CO_2$ and CO in relative humidity levels in the range of 25 – 75 % and operating temperatures ranging from 300 – 400 °C. Influencing factors like humidity and sensor operating temperature on the sensor response are examined.

# Abstract (Deutsch)

Gassensoren haben ein hohes Potential für zahlreiche innovative Anwendungen, die von der Überwachung der Luftqualität in Räumen und Gebäuden (Smart Home) bis hin zum Umwelt Monitoring mittels Smartphone oder der Früherkennung von Krankheiten durch Atemluftanalyse (Smart Health) reichen. Für diese Anwendungen müssen Gassensoren eine ausreichende Empfindlichkeit (= Sensitivität) aufweisen, vor allem aber müssen sie in der Lage sein, ein bestimmtes Gas gezielt aus einem Gasgemisch detektieren zu können (= Selektivität).

Eine Vielzahl von Gassensoren basierend auf verschiedenen Detektionsmechanismen wurde in den letzten Jahrzehnten entwickelt. Chemieresistive Sensoren stellen dabei die bei weitem dominierende Klasse von Gassensoren dar: Bei diesen Sensoren wird der elektrische Widerstand eines gassensitiven Materials durch Wechselwirkung mit einem Gas geändert, wodurch sich eine direkte elektronisch auswertbare Messgröße ergibt. Als gassensitives Material werden dabei häufig halbleitende Metalloxide eingesetzt.

Im Rahmen dieser Arbeit wird ein p-Typ Halbleitermaterial, nämlich Kupfer(II)oxid als dünne Schicht auf Silizium Wafern abgeschieden. Die Kupfer(II)oxid Dünnschichten werden durch unterschiedlich konzentrierte Kupfernitrat-, Kupferchlorid- oder Kupferacetat-Ausgangslösungen mithilfe der Spray Pyrolyse Technik abgeschieden. Der Einfluss der Ausgangslösung, Sprühzeit, Abscheidetemperatur und der Abstand zwischen Sprühkopf und Substrat wird dabei erforscht. Die Filme werden mit unterschiedlichen Analysemethoden charakterisiert und anschließend photolithografisch strukturiert. Die strukturierten Dünnschichten werden für den Zusammenbau der Gassensoren verwendet, welche anschließend auf ihre Sensitivität gegenüber $CO_2$ und CO untersucht werden.

# Acknowledgements

The presented work was conducted at the Materials Center Leoben Forschung GmbH (MCL, department Materials for Microelectronics). Financial support is acknowledged from the project "FunkyNano - Optimierte Funktionalisierung von Nanosensoren zur Gasdetektion durch Screening von Hybrid-Nanopartikeln" (Österreichische Forschungsförderungsgesellschaft FFG, Grant No. 858637).

First of all, I would like to thank Anton Köck, who gave me the opportunity to work on an exciting and multifaceted topic. I would also like to express my appreciation for the warm welcome to his work group. I would like to thank him for the competent guidance and the trust in my work. Furthermore, I want to thank Robert Wimmer-Teubenbacher for supporting me not only with experimental procedure but also during the writing process of this thesis. I would like to thank him for valuable discussions and helpful advices at any time. Special thanks go to my colleague Florentyna Sosada-Ludwikowska for her amazing helpfulness and for always being ready to answer my questions. Moreover, I want to thank Marco Holzer for Raman characterizations and for greatly appreciated motivating words when needed.

I would like to thank Verena Leitgeb for AFM characterizations and Jaroslaw Wosik for providing SEM images. Also, I am grateful to Paul Angerer and Bernhard Friessnegger for their valuable time on XRD measurements and discussions.

In addition, I am very thankful to all other colleagues at the Materials for Microelectronics department at MCL for creating an enjoyable and relaxing work atmosphere.

Moreover, I would like to thank my family and friends with all my heart for their constant encouragement and support throughout my university education.

Last but not least, I would like to thank my partner Martin, who constantly supports me and believes in me. I am grateful for his help with XRD plots, the many fruitful scientific discussions, and highly appreciated advices he gave me during this thesis. But I especially would like to thank him for his incredible patience, support and faith in me at any time.

# Content

# 1. Introduction

Monitoring the concentration of gases has become an important requirement in many industrial processes as well as in daily life. Accordingly, an increased interest in gas sensitive materials and the thereof made gas sensors has evolved.

The goal of the project FunkyNano is the development of a screening platform for optimizing metal oxide semiconductor gas sensors with functional nanoparticles. The FunkyNano screening platform is based on nanosensor arrays employing three different metal oxide semiconductor thin films: tin dioxide ($SnO_2$), zinc oxide (ZnO) and copper oxide (CuO). While the deposition processes for $SnO_2$ and ZnO films have been already established in previous work, development of the CuO deposition process is of high importance to enable the full screening of all three metal oxide types within the FunkyNano project. Moreover, CuO has proven as highly promising material for the realization of $CO_2$ gas sensors.

The goal of this thesis is therefore the development of a reliable spray pyrolysis based technology for the deposition of gas sensitive CuO thin films.

## 1.1. Application of Gas Sensors

Historically, gas sensors first appeared in the mining industry for monitoring hazardous gases [1]. They were used for continuous monitoring of $O_2$ levels in coal mines and detection of the highly explosive gas methane [2]. For these reasons, they have been playing an important role for the miner's worksite safety.

Over the last decades, the need for gas sensitive devices has increased extensively. These gas sensitive devices need to be precise and reliable, since differentiation between low gas concentrations is desirable. Typical gases of interest are CO, $CO_2$, volatile organic compounds (VOCs), NO, $NO_2$, $O_3$, $CH_4$ and other hydrocarbons [1,3].

Nowadays, gas sensors have found a broad range of applications. They appear in air quality control systems, in the medical sector and in food industry [4]. Due to this variety of applications, an extensive research field has evolved.

Indoor gas sensor applications include toxic and flammable gas alarm systems [5], smoke detection [6], odors and humidity monitoring, and heating, ventilation and air conditioning (HVAC) [7]. These numerous applications gave rise to an increasing demand for air quality gas sensors [7].

Many of these applications are based on the detection of $CO_2$; e.g. the control and correct adjustment of $CO_2$ levels in air conditioned buildings could save around 40 % of required energy [8]. Furthermore, good air quality correlates with physical well-being and human health. Since most of us spend a tremendous amount of our lifetime indoors, indoor air quality control is becoming increasingly important.

Furthermore, outdoor air quality control is gaining much attention due to steadily growing atmospheric pollution caused by combustion of fossil fuels and exhausts from industrial plants. In the fields of outdoor air quality control, gas sensors are already well established [7].

Apart from that, a steadily growing market for gas sensors in the medical sector has developed. According to Kim *et al.* [9] exhaled breath analysis is becoming an increasingly important method for evaluation of health status or clinical diagnosis of various diseases. Diabetic patients, for instance, exhale a certain amount of acetone, which is a VOC and can be determined by breath analysis. In addition, specific amounts of alkanes or aromatic compounds in the human breath are known to be indicators of lung cancer.

Furthermore, the application of gas sensors plays an important role in food industry, due to possible detection of food contaminants such as preserving agents, antibiotics, heavy metal ions, toxins, microbial load and pathogens [4].

Considering the many applications of gas sensors, extensive efforts are made not only for advancing already established sensors but also for developing various new gas sensors [7].

## 1.2. Band Theory of Solids

According to the band theory of solids, there are three main classes of materials: conductors, insulators and semiconductors (Figure 1). These three classes can be differentiated by the electron occupation of their orbitals.

While a single atom exhibits discrete electron shells, a solid state behaves different: When atoms are packaged close together, such as in a crystal, the electron shells interact and form energy bands (valence and conduction band). Valence and conduction band are the bands closest to the Fermi level, which is defined as the highest occupied electron state at a temperature of absolute zero [10].

Electrical conductivity depends on the ability for the valence and conduction band to exchange electrons. In metals (e.g. Al, Cu, Ag and Au) these two bands overlap, allowing an easy and fast electron exchange. Metals show high electrical conductivity and are called conductors.

In contrast to conductors, insulators like $SiO_2$ are characterized by a large band gap of 8.9 eV [11]. The band gap is caused by a broad range of unallowed electronic states, which makes electrons hardly moveable. Insulators show no electrical conductivity, since they prevent electron exchange between valence and conduction band.

Semiconductors (e.g. Si, C, Ge, $SnO_2$, ZnO and CuO) are in between conductors and insulators. Semiconductors have a smaller band gap than insulators. A typical value for the Si energy band gap is 1.1 eV [11]. With sufficient energy input in the form of thermal energy, photoenergy or radiation, some electrons can overcome the band gap. As a result, valence and conduction band can exchange electrons and electrical conductivity increases.

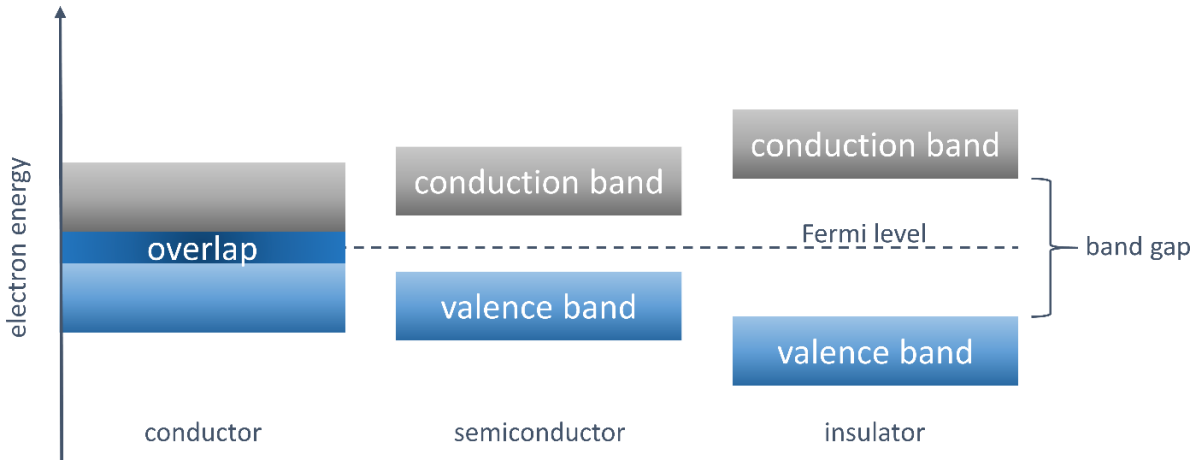


*Figure 1: Schematic band diagrams of conductor, semiconductor and insulator.*

Semiconductors can be classified based on the type of dominating charge carriers. The two different types of charge carriers are electrons and holes. Electrons carry a negative electric charge, whilst holes carry a positive electric charge. The hole's positive charge is caused by an electron vacancy in the atom's crystal lattice. In a typical crystal lattice, the negative charge of the electrons is balanced by the positive nucleus of the atom. However, an electron vacancy leaves behind a positive net charge at the holes's position.

Based on the type of dominating charge carriers, semiconductors can be classified into n-type or p-type materials [2]. Materials with a majority of negative charge carriers (electrons) are called n-type semiconductors, whilst those with a majority of positive charge carriers (holes) are called p-type semiconductors [12],[13]. Common examples for n- and p-type MOS are listed in Table 1.

*Table 1: Examples for n-type and p-type metal oxide semiconductors [14].*

| Conduction type | Metal oxide semiconductor |
|---|---|
| **n-type** | $SnO_2$, $WO_3$, ZnO, $TiO_2$, $ZrO_2$, $In_2O_3$, $Fe_2O_3$, $La_2O_3$ |
| **p-type** | CuO, NiO, $Cr_2O_3$, $Co_3O_4$ |

## 1.3. Metal Oxide Semiconductor Gas Sensors

Over the past five decades, a vast variety of gas sensors has been developed for monitoring various analytes. In general, gas sensors can be classified based on their detection mechanism and the type of gas sensitive materials used in their manufacturing process [1]. Conventional analytical techniques such as optical spectroscopy or gas chromatography are costly and time-consuming. Furthermore, optical spectroscopy and gas chromatography devices need much space due to their complex construction. However, the global trend is going to miniaturized, high performance devices that are cheap in production and can be scaled up to industrial dimensions.

According to Barsan *et. al.* [5] one of the most promising sensor technologies providing small, cheap and high performance devices uses metal oxide semiconductors (MOS) as gas sensitive material. From the chemical point of view, MOS are ionically bonded solids that consist of positively charged metal ions and negatively charged oxygen ions [4]. The gas measuring principle is based on a chemical interaction of the metal oxide surface with the surrounding gas, resulting in a change of electrical conductivity of the metal oxide [2] (explained in detail in chapter *Ionosorption of Atmospheric Gases at MOS Surface*).

Generally, these chemical reactions include adsorption and desorption processes of gas molecules at the metal oxide surface at elevated temperatures, usually ranging from 200 – 400 °C. During exposure to gas, changes in the electrical conductivity of the metal oxide are monitored.

Nowadays, rigorous efforts are in progress to find suitable metal oxide semiconductor materials. This type of gas sensitive material is used in conductometric gas sensors and offers many benefits like:

- reduced size and weight,
- comparatively low power consumption,
- fast response,
- the possibility of cheap and flexible production processes in combination with industrial up-scaling
- and high sensitivity to a broad range of gases.

At the same time, the high sensitivity to various gases results in low selectivity between those gases. However, the insufficient selectivity between gases is one of the main problems [2] of all the state-of-

the-art gas sensors on the market. Sensors show a cross sensitivity to humidity and other gases. Furthermore, specific target gases, like $CO_2$, cannot be detected at all.

The goal of the project FunkyNano is the development of a screening platform for optimizing gas sensors with functional nanoparticles. It is well known that the functionalization of gas sensors with nanoparticles leads to an improvement in the selectivity but so far has not been implemented in common practice yet. Nanosensor arrays are fabricated using different gas sensitive metal oxide thin films, which are functionalized by inkjet printing with various nanoparticles, where concentration and combination of the nanoparticles are systematically modified.

## 1.4. Ionosorption of Atmospheric Gases at MOS Surface

According to Fine *et. al.* [10] an interaction of the target gas with the surface of the MOS results in a change in charge carrier concentration of the MOS material. As a result, the conductivity of the MOS material changes. In order to understand the exact gas sensing mechanism, the processes at the solid-gas interface need to be examined [15]. It is assumed that ambient oxygen is adsorbed on the MOS surface in a process called ionosorption [16]. Ionosorption is the chemisorption of ions, where the adsorbate is bonded to the surface by an electrostatic interaction [15]. In principle, oxygen is ionosorbed as molecular oxygen ion ($O_2^-$) or atomic oxygen ions ($O^{2-}$, $O^-$) at the MOS surface [17].

In case of molecular oxygen ions, $O_2$ adsorbs to the MOS surface and draws an electron from the MOS to form $O_2^-$ (Eq. 1 and 2). In case of atomic oxygen ions, the adsorbed $O_2$ molecule is dissociated into two oxygen atoms (Eq. 1). These oxygen atoms draw an electron from the MOS to form $O^-$ (Eq. 3) [15]. If $O^-$ attracts another electron, $O^{2-}$ is formed (Eq. 4).

The molecular oxygen ions are dominating at temperatures below 200°C, whilst the atomic oxygen ions are mainly present at temperatures above 200°C [18].

$$O_{2(gas)} \leftrightarrow O_{2(ads)} \leftrightarrow 2\,O_{(ads)} \quad \text{Eq. 1}$$

$$O_{2(ads)} + e^- \leftrightarrow O^-_{2(ads)} \quad \text{Eq. 2}$$

$$O_{(ads)} + e^- \leftrightarrow O^-_{(ads)} \quad \text{Eq. 3}$$

$$O^-_{(ads)} + e^- \leftrightarrow O^{2-}_{(ads)} \quad \text{Eq. 4}$$

The adsorbed oxygen species extract electrons from the conduction band, which induces a negatively charged surface. The growing negative surface charge acts repulsively on electrons, which try to fill surface states (oxygen adsorption). At a certain surface charge, the kinetic energy of the electrons is insufficient to overcome the repulsive surface potential. A space charge layer is formed between the surface and the bulk of the MOS. In case of n-type materials, the space charge layer is called electron depletion layer, since this layer is depleted of electrons. In case of p-type materials, the space charge layer is called hole accumulation layer, since holes of the valence band are attracted to the negative surface potential.

In the energy band diagrams (Figure 2) the space charge layer is represented by the band bending of the valence and conduction band [18]. In n-type materials, the charge carriers of the conduction band are reduced; therefore electron transport from the bulk to the surface decreases. In p-type materials, accumulation of charge carriers is observed due to captured electrons from the valence band [8].

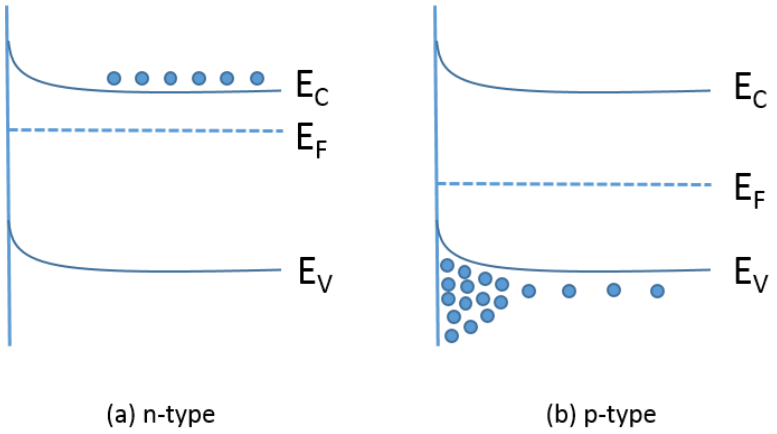


*Figure 2: Energy bands of (a) n-type and (b) p-type semiconducting metal oxides with $E_C$ = conduction band, $E_F$ = fermi level and $E_V$ = valence band; adapted from [8].*

## 1.5. Interaction of Adsorbed Species with Target Gas

The adsorbed oxygen species interact with the surrounding gas and influence the charge carrier concentration of the MOS. This in turn influences the band bending resulting in a change of the material's conductivity [8]. Depending on whether the target gas is a reducing (e.g. C, CO, $CH_4$, $H_2$) or oxidising gas (e.g. NO, $NO_2$), different surface reactions occur and consequently conductivity increases or decreases.

In n-type semiconductors, reducing gases remove some of the adsorbed oxygen species forcing electrons to move back into the MOS. The negative charge carrier concentration increases, the electron depletion layer decreases and conductivity increases. Conversely, an oxidising gas decreases

the negative charge carrier concentration. The electron depletion layer increases and conductivity decreases [10].

In p-type semiconductors, the opposite effects are observed. Interaction with a reducing gas introduces additional negative charge into the material and reduces the positive charge carrier concentration. As a result, conductivity decreases. Interaction with an oxidising gas, increases the positive charge carrier concentration and conductivity increases [10].

An overview of changes in conductivity is given in Table 2.

*Table 2: Changes in conductivity (increase or decrease) of metal oxide semiconductors (n- or p-type) by interaction with reducing or oxidising gas [19].*

| **Conduction type** | **Reducing gas** | **Oxidising gas** |
|---|---|---|
| **n-type** | Conductivity increase | Conductivity decrease |
| **p-type** | Conductivity decrease | Conductivity increase |

Equations 5 -7 show the interaction of ionosorbed oxygen species with CO (reducing gas). In these reaction mechanisms gaseous $CO_2$ and electrons are formed. The formed electrons are released into the conduction band [8].

$$2\,CO + O_{2(ads)}^{-} \leftrightarrow 2\,CO_2 + e^{-} \quad \text{Eq. 5}$$

$$CO + O_{(ads)}^{-} \leftrightarrow CO_2 + e^{-} \quad \text{Eq. 6}$$

$$CO + O_{(ads)}^{2-} \leftrightarrow CO_2 + 2\,e^{-} \quad \text{Eq. 7}$$

While reducing gases generate electrons, oxidizing gases (such as $NO_2$), react with electrons from the MOS (Eq. 8) [2].

$$NO_{2(ads)} + e^{-} \leftrightarrow NO_{2\,(ads)}^{-} \quad \text{Eq. 8}$$

## 1.6. MOS Gas Sensors and CMOS Integration

Typically, MOS gas sensors in industrial processes are based on thick films of sensitive material. These rather bulky gas sensitive devices are costly and have a high power consumption. In order to minimize size, cost and power consumption, combinations of thin layers of sensitive material with low-cost manufacturing technologies are desired. One of the key features is the integration of MOS materials with so-called complementary metal oxide semiconductors (CMOS) devices. CMOS technology is the core of microelectronic fabrication enabling mass production of modern microchip devices. Combining

metal oxide materials with CMOS technology could reduce device size and power consumption extensively. However, to the best of the author's knowledge, no viable and cost-efficient MOS gas sensors implemented in CMOS technology are commercially available so far.

Hence, the key research focus of this thesis is on the fabrication of p-type semiconductor thin films, namely cupric oxide (CuO), as sensitive material for CMOS compatible gas sensors.

## 1.7. Thin Film Deposition via Spray Pyrolysis Technique

The application of thin films in modern technologies is widespread. Generally, thin films can be fabricated by different deposition processes (Figure 3), which are either of physical or chemical nature. These types of thin film deposition processes can be further divided into subbranches. Examples of physical deposition processes include sputtering and evaporation processes. Chemical deposition processes rely on either a fluid or gaseous precursor. Among the chemical deposition processes based on gaseous precursors, chemical vapor deposition (CVD) is the main representative. Those based on liquid precursors include sol-gel, spin coating, drop coating, dip coating and spray pyrolysis [20]. However, spray pyrolysis is sometimes referred as CVD process since the precursor solution is vaporized at high operating temperatures. There are of course further numerous examples of thin film deposition processes, which are not listed in Figure 3.

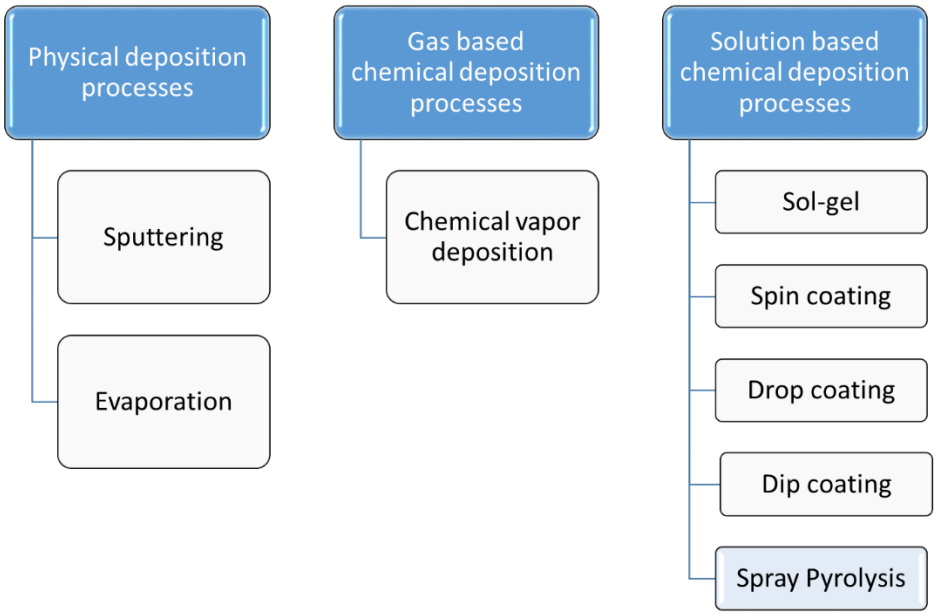


*Figure 3: Overview of different thin film deposition processes based on physical or chemical nature.*

Spray pyrolysis is a process in which a precursor solution is sprayed onto a heated substrate in order to deposit a thin layer. In order to atomize the liquid precursor into a fine mist, a specific pressure must be applied. The precursor solution is atomized by means of $N_2$ into very fine droplets, which then hit the pre-heated substrate, chemically react and form a thin layer of deposited material.

A typical pneumatic spray pyrolysis unit (depicted in Figure 4) mainly consists of

- a precursor solution reservoir,
- an air atomizing nozzle,
- a substrate heater,
- a temperature controller,
- and gas supply with pressure regulation.

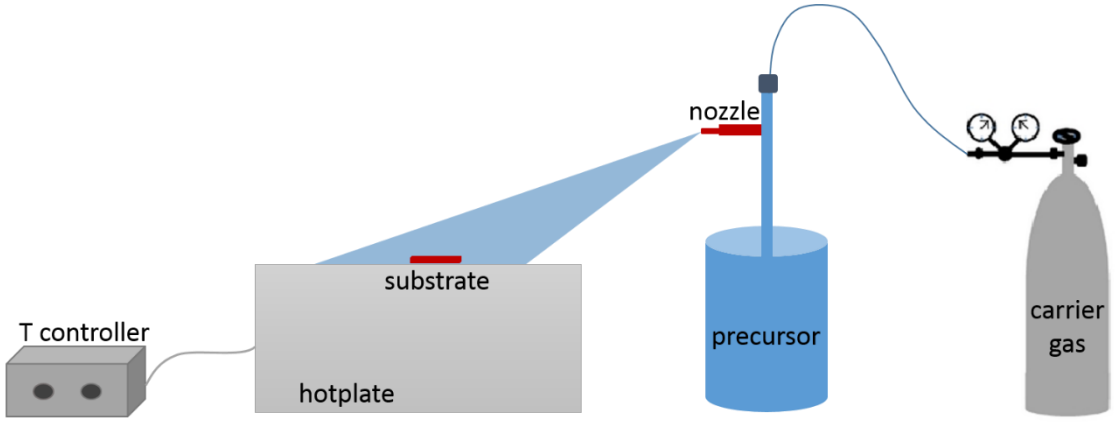


*Figure 4: Schematic sketch of a spray pyrolysis set up.*

Compared to other deposition processes, spray pyrolysis offers various benefits for the deposition of thin films. Among the benefits are

- the simplicity of apparatus,
- low cost,
- fast deposition procedure,
- easy controllability of layer thickness,
- operation at moderate temperatures (usually 100 – 500°C),
- no need for vacuum,
- easy doping of films by variation of precursor solution,
- a broad range of deposition material,
- and good productivity on large scale.

To sum up, the equipment is simple and precursor materials are cheap, which makes spray pyrolysis an inexpensive deposition method and suitable for industrial scale-up.

Thin film deposition via spray pyrolysis is influenced by various parameters including deposition temperature, droplet size, gas flow and the distance between nozzle and substrate. Furthermore, the used precursor solutions, their concentration and solvents play an important role.

Among all these influencing factors, deposition temperature is one of the most influential one. Viguie and Spitz [21] suggested four different film growth mechanisms for the spray pyrolysis process depending on the deposition temperature (Figure 5). At the lowest temperature (process A), the droplet directly impinges onto the substrate and decomposes. At higher temperatures (process B), the solvent evaporates before reaching the substrate and dry precipitate pyrolyzes after hitting the substrate. At even higher temperatures (process C), the solvent evaporates leaving behind a solid precipitate which melts and vaporizes. The vapor diffuses to the substrate undergoing a CVD process. At the highest temperature (process D), the precursor material decomposes and forms solid particles before hitting the substrate.

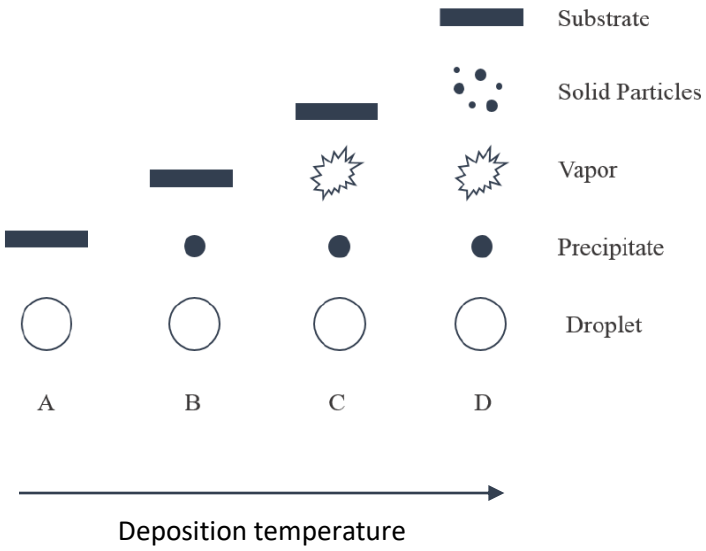


*Figure 5: Possible reaction sequences during spray pyrolysis depending on deposition temperature; adapted from [19]*

According to Perednis and Gauckler [20], process A, B and D can lead to rough or non-adherent films, while process C enables deposition of high quality adherent films.

# 2. Fabrication of Silicon Based CuO Thin Film Gas Sensors

The experimental goal of this thesis is to fabricate gas sensors based on CuO thin films as sensitive material. To achieve it, several experimental steps are needed ranging from the deposition of CuO thin films via spray pyrolysis, to photolithography, to etching and photoresist removal, up to the final assembly of the gas sensors. In the following chapter, these experimental steps will be explained in detail.


*Scheme 1: Overview of experimental steps ranging from thin film deposition up to the final gas sensor.*

## 2.1. CuO Thin Film Deposition

In this work, CuO thin films were deposited on Si wafer with an insulation layer of $SiO_2$ on top and on Si wafer with an incorporated electrode system for realization of gas sensor structures (so called FunkyNano platform chips, shown in Figure 6). Both substrates were processed by ams AG and exhibit a size of 2x2 cm. The FunkyNano platform chips consist of Si as base material, 1000 nm $SiO_2$ as insulation layer, 5 nm titanium as an adhesion layer and platinum electrodes with a thickness of 200 nm for resistance measurements. Since the electrode system is needed for resistance measurements of the sensor material, FunkyNano platform chips instead of bare Si substrates were used for further fabrication of silicon based CuO thin film gas sensors.

*Figure 6: 2x2 cm FunkyNano platform chip: Si + 1000 nm $SiO_2$ + 5 nm Ti + 200 nm thick Pt electrodes*

The spray pyrolysis process was carried out at the Materials Center Leoben (MCL) Microelectronic laboratory. For better visualization, the experimental set up is shown in Figure 7. The used equipment constitutes of:

- a high-temperature titanium hotplate (PZ28-3T, Harry Gestigkeit GmbH) for heating the $SiO_2$ substrates,
- a temperature controller (PR5 3T, Harry Gestigkeit GmbH) which allows fast and accurate heating of the hotplate,
- a precursor solution reservoir,
- an air atomizing nozzle (Quickmist 1/4QMJ with a flat air cap SUQR220B) for atomizing the precursor solutions into fine droplets
- and a gas supply with pressure regulation.

The air inlet was equipped with a switch for an easy start and stop of the spraying process. As carrier gas, $N_2$ was used.

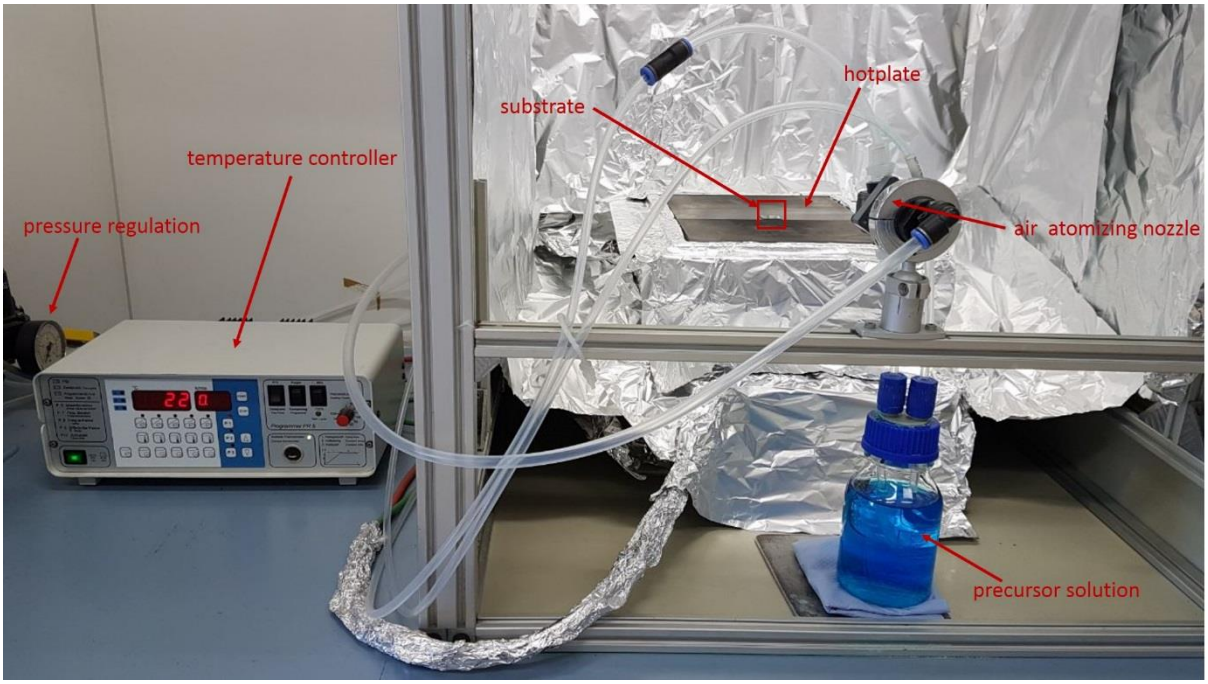


*Figure 7: Spray pyrolysis set up in the MCL microelectronic lab.*

CuO thin films can be fabricated by different chemical approaches [22–24] employing different precursor solutions consisting of:

- Cu-nitrate,
- Cu-chloride,
- or Cu-acetate.

In this thesis, the three different precursor solutions were prepared by dissolving a specific amount of

- $Cu(NO_3)_2 \times 3H_2O$ (puriss. p.a., 99-104%, Sigma-Aldrich),
- $CuCl_2 \times 2H_2O$ (ACS reagent, ≥99.0%, Sigma-Aldrich)
- or $Cu(CH_3COO)_2 \times H_2O$ (ACS reagent, p.a., ≥99.0%, Carl Roth GmbH + Co. KG)

in distilled water. The reaction pathways of CuO deposition based on the different precursors are shown in equations 7 - 9.

$$Cu(NO_3)_2 + H_2O \rightarrow CuO + 2\,HNO_3 \quad \text{Eq. 7}$$

$$CuCl_2 + H_2O \rightarrow CuO + 2\,HCl \quad \text{Eq. 8}$$

$$Cu(CH_3COO)_2 + H_2O \rightarrow CuO + 2\,CH_3COOH \quad \text{Eq. 9}$$

For further simplification in this thesis, the Cu-nitrate, Cu-chloride and Cu-acetate precursor solutions are called $CuNit_2$, $CuCl_2$ and $CuAc_2$, respectively.

The deposition behavior is however not only influenced by the used precursor solution, but also by different deposition parameters. Trying to find the optimal spray pyrolysis set up, different combinations of deposition parameters were tried:

- spray time was varied from 2 – 20 min,
- the concentration of the precursor solutions was varied from 0.05 M to 0.3 M,
- the hotplate temperature was varied from 250 – 400 °C,
- different solvents were used,
- and the substrate position on the hotplate was changed in order to optimize the nozzle to substrate distance.

The following chapters give an overview of the deposition behavior influenced by deposition parameter variation. It focuses on general deposition behavior, independent from the used precursor solution ($CuNit_2$, $CuCl_2$ and $CuAc_2$). The influence of the used precursor itself, will be explained in the chapter *Thin Film Characterization*.

## Spray Time and Precursor Concentration Dependency

Spray time is one of the most important influencing parameters for thin film deposition via spray pyrolysis. To observe the effects of spray time on the deposition behavior, substrates were spray coated for 2 – 20 min. The longer a precursor solution is sprayed onto the heated substrate, the more material is deposited. This trend of higher deposition at longer spray time was seen independently

from the precursor solution; deposition increased with increasing spray time, regardless on which precursor solution was used.

Furthermore, the effects of precursor concentration on the deposition behavior were examined. Precursor concentration was varied from 0.05 – 0.3 M. The higher the precursor concentration, the more reactive material hits the substrate surface. The reactive material is undergoing a chemical reaction at the substrate surface, while forming a thin film on it. Accordingly, the highest deposition rate was obtained by using 0.3 M precursor solutions.

Figure 8 qualitatively shows the effects of spray time and precursor concentration variation on the deposition behavior. CuO thin films fabricated at 400 °C with $CuCl_2$ precursor solutions (0.05, 0.1, 0.2 and 0.3 M; increasing from top to bottom) at different spray times (3, 5 and 7 min; increasing from left to right) are shown. The deposition rate increases as the spray time and the precursor concentration increases. This trend was not only justified for $CuCl_2$ but also for $CuNit_2$ and $CuAc_2$ precursor solutions.

In case of 0.05 M precursor solution and 3 min spray time, low deposition is obtained. In case of 0.3 M precursor solution and 7 min spray time, high deposition is obtained. This is mainly related to the high amount of reactive species, forming CuO on the substrate surface.

For optimal thin film deposition, a spray time of 10 min and a precursor concentration of 0.3 M was selected.

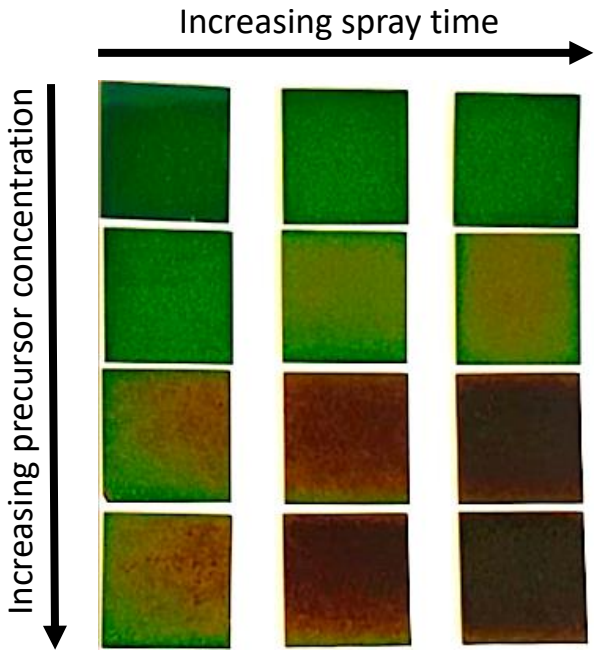


*Figure 8: CuO thin films fabricated at 400 °C with $CuCl_2$ precursor solutions (0.05, 0.1, 0.2, 0.3 M; increasing from top to bottom) at different spray times (3, 5, 7 min; increasing from left to right).*

## Temperature Dependency

CuO thin films were deposited at 250, 300, 350 and 400°C. In order to ensure integration with CMOS fabricated microhotplate chips, 400 °C is the maximum allowed temperature for such CMOS chips.

In terms of temperature variation, every of the three precursor solutions followed the same trend. This trend showed higher deposition rate at higher temperatures. In case of 250 °C, only few amounts of CuO were deposited. In case of 400 °C, high amounts of deposited CuO were observed. Due to the higher deposition rate and resulting film thickness increase at higher temperatures, 400 °C was selected as optimal hotplate temperature for further CuO depositions.

## Substrate to Nozzle Distance

Atomizing the precursor solution gives a stream of differently-sized droplets. Depending on the substrate position on the hotplate, different sizes and quantities of droplets hit the substrate surface. Droplet size decreases from the middle to the outer part of the stream. Whilst many droplets are present in the middle of the precursor stream, fewer droplets are observed at the outer parts of the stream.

Goal of the deposition process was to find the perfect substrate position on the hotplate, in order to achieve high amounts of perfectly sized droplets hitting the substrate surface. Therefore, horizontal as well as vertical distance between nozzle and substrate had to be optimized. Through experimentations, an optimal horizontal distance of 33 cm and a vertical distance of 6 cm was determined.

## Solvent Dependency

The used precursor solutions consisted of Cu salts dissolved in water. Water has a high surface tension ($\gamma$ = 72.8 mN/m at 20 °C) [25] because of the relatively high attraction of water molecules to each other. Other liquids instead, e.g. ethanol, have lower surface tension ($\gamma$ = 22.3 mN/m at 20 °C) [25]. Assuming better precursor adhesion on the substrate surface due to lower surface tension, a certain amount of water was replaced by ethanol (≥99.8 %; Carl Roth GmbH + Co. KG). Subsequently, deposition experiments were carried out with five different water to ethanol ratios (Table 3).

*Table 3: Ratio of DI water to ethanol in vol%.*

| Solution | Vol% DI water | Vol% ethanol |
|---|---|---|
| **1** | 100 | 0 |
| **2** | 70 | 30 |
| **3** | 50 | 50 |
| **4** | 30 | 70 |
| **5** | 10 | 90 |

Although better precursor adhesion to the substrate surface was expected, no significant change in CuO deposition could be observed by varying the precursor solvent. Since the replacement of water by ethanol did not make a difference, DI water was maintained as solvent.

The three precursor solutions are highly soluble in water. However, complete dissolving of small particles could not be guaranteed. In order to avoid solid particles in the precursor solutions, solutions were filtered before sprayed onto the substrate (filtrate bottle, Thermo Scientific; MN 85/70 filters, Macherey-Nagel). The filtered precursor solution, however, didn't show an optical difference compared to the unfiltered solutions. After spraying, distinction between CuO thin films sprayed with filtered and unfiltered precursor solution was not possible. Hence, it is assumed that filtration of the precursor solution does not result in an advantage for CuO thin film deposition and therefore solutions were no longer filtered before spraying.

## Optimal Deposition Parameters

Deposition parameters for CuO thin film deposition were optimized experimentally via interpretation in the optical microscope. Table 4 summarizes the optimal deposition parameters including those experimentally determined and those fixed (pressure regulation). In this case, optimum means a homogeneous film thickness and a minimum amount of bigger agglomerates.

*Table 4: Optimal spray pyrolysis set up parameters for CuO thin film deposition.*

| **Parameters** | |
|---|---|
| **Precursor solution** | 0.3 M $CuAc_2$ |
| **Solvent** | $H_2O$ |
| $\mathbf{p_{N2,\ flask}}$ | 1.0 bar |
| $\mathbf{p_{N2,\ atomization}}$ | 0.3 bar |

| | |
|---|---|
| $p_{compressed\ air}$ | 1.1 bar |
| **Horizontal sample to nozzle distance** | 33 cm |
| **Vertical sample to nozzle distance** | 6 cm |
| **Substrate temperature** | 400 °C |
| **Spray time** | 10 min |

## 2.2. Photolithography

After deposition of the CuO thin films by spray pyrolysis, the next step in the gas sensor fabrication was patterning the CuO layer by photolithography. The photolithography steps were carried out either at Montanuniversität Leoben (MUL) at the Department of Polymeric Engineering and Science, or at the Austrian Institute of Technology (AIT) in Vienna. In general, eight steps (Scheme 2) were needed, ranging from deposition of the photoresist by spin coating up to the patterned CuO thin film. Those steps were the same, both at MUL and AIT.

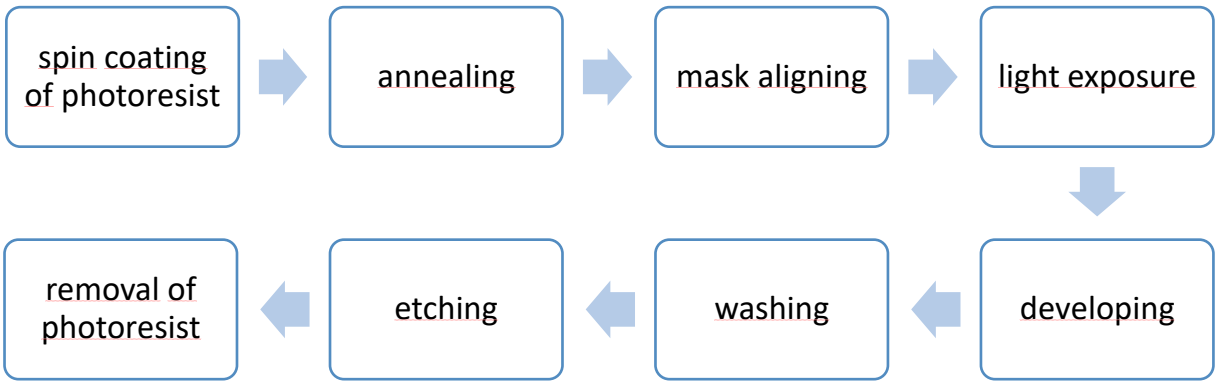


*Scheme 2: Process scheme of photolithographic steps including etching and removal of photoresist.*

After deposition of CuO by spray pyrolysis, a positive photoresist (AZ MIR 701, MicroChemicals GmbH) was spincoated onto the CuO thin film samples for 30 s at 4000 rpm and an acceleration rate of 5000 rpm/s (Spin Coater Model 4000, Electronic Micro Systems LTD). The photoresist was applied as a rectangular area of 200 x 100 nm (shown in the upper third of Figure 9) in order to protect this specific position from being etched. Subsequently, the samples were annealed at 100°C for 60 s. For pattering the CuO layer, a photolithography mask was adjusted to the sample's surface by means of a manual mask aligner MJB4 (Suss Microtec). UV irradiation was done in soft contact mode for 13.1 s with a light

intensity of 13.6 W/m$^2$. The photoresist was developed (AZ 726 MIF Developer, Merck) for 60 s and the patterned samples were washed with DI $H_2O$.

The photolithography steps at AIT were almost the same as at MUL. The same photoresist (AZ MIR 701, MicroChemicals GmbH) was spincoated onto the samples for 35 s at 4000 rpm (Ramgraber GmbH Spin Coater) to obtain a resist thickness of 1.1 µm. After annealing for 60 s at 100°C the photolithography mask was aligned by means of an EVG620 mask aligner in hard contact mode. UV irradiation was done with an exposure dose of 70 mJ/cm$^2$. The photoresist was developed (AZ 726 MIF Developer, Merck) for 60 s and the patterned samples were washed with DI $H_2O$.

The rectangular area of photoresist assured CuO thin films at specific positions on the FunkyNano platform chip. The CuO thin films at these specific positions provided a contact to the incorporated electrode system on the chip via Pt electrodes. The Pt electrodes are depicted in Figure 9 as straight lines ranging from the rectangular photoresist area to the lower part of the image. Allowing resistance measurements of CuO films, Pt electrodes are used to electrically contact the CuO films in a 4 point configuration.

Some photoresist rests remained at undesired positions, visible left to the rectangular area in Figure 9. This can be explained by possible contamination of the photolithography mask preventing light exposure at some positions on the thin film. However, the remaining CuO rests did not influence the following gas sensing experiments.

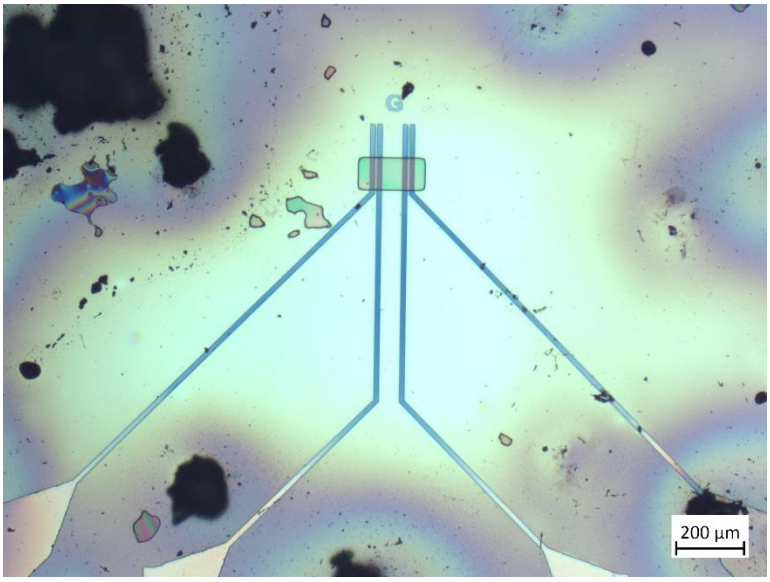


*Figure 9: Light microscope image of a CuO thin film deposited for 10 min with 0.1 M $CuAc_2$ precursor solution on a FunkyNano substrate. The thin film is covered by a rectangular area of photoresist, shown in the upper third of the picture.*

## 2.3. Etching

### Chemical Wet Etching

In order to remove the CuO thin film from areas not protected by photoresist, chemical wet etching with HCl (ACS reagent, 37%, Sigma-Aldrich), $HNO_3$ (ACS reagent, ≥90.0%, Sigma-Aldrich), $H_2SO_4$ (ROTIPURAN® 98%, Roth) or HI (57 wt%, 99.95%, Sigma-Aldrich) in different concentrations was performed. The etching rate could be controlled by varying the acid concentration and etching time. After etching, the photoresist was removed by dipping the samples into acetone for 10 min. As a result, CuO structures only remained on positions, which had been covered by photoresist before.

The etching experiments were performed on CuO thin films deposited with $CuNit_2$, $CuCl_2$ and $CuAc_2$ precursor solutions of different concentrations (0.5 – 0.3 M). All four acids (HCl, $HNO_3$, $H_2SO_4$ and HI) revealed good etching capability since the remaining CuO structures on the substrate were sharp and clearly visible. HCl revealed the best etching capability, compared to the other mentioned acids, and was used for further etching experiments. Therefore, a concentration of 6 M and an etching time of 5 – 7 min, depending on the layer thickness, was used.

Figure 10 shows the etching process ranging from the CuO thin film covered by a rectangular area of photoresist (left), to the etched CuO nanostructure still covered by photoresist (middle), up to the remaining CuO nanostructure after removal of the photoresist (right). After an etching period of roughly 5 min, underetching was observed at the transition from the Si substrate to the Pt electrodes. However, the CuO nanostructure still covered the four Pt electrodes, providing an electrical contact.

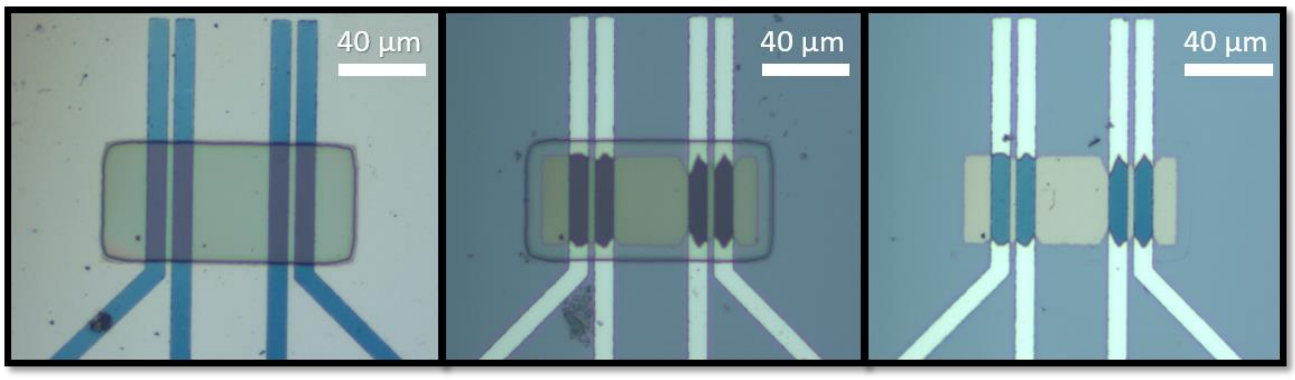


*Figure 10: CuO thin film covered by photoresist (left), etched CuO nanostructure still covered by photoresist (middle) and remaining CuO nanostructure after removal of photoresist (right).*

## Argon Ion Etching

Alternatively to chemical wet etching, dry physical etching with Ar ions (IonSys 500, Roth und Rau AG) was employed at AIT to remove the excess CuO thin film. This process is the technology of choice for structuring the $SnO_2$ thin films fabricated at MCL.

The samples were mounted in the middle of the substrate holder (Figure 11), which was then fixed in the vacuum chamber of the ion etcher. The operation pressure during etching was $2\times10^{-6}$ mbar and the beam voltage was 500 V. A cycle of Ar ion etching included 8 x 1 min etching with a pause of 2 min in between. Several etching cycles with an overall etching period of approximately 60 min were performed trying to etch the CuO films. However, etching of CuO films deposited for 10 min with 0.1 M $CuAc_2$ precursor solution was not accomplished. Even though CuO thin films showed slight optical differences in the form of reduced film thickness after etching, removal of the complete CuO thin film was impossible. It is assumed that etching time was too short and beam voltage too low. When comparing argon ion etching to chemical wet etching, the latter is much more efficient. However, this process will be repeated again, because basically the etching of CuO with argon ions should be feasible.

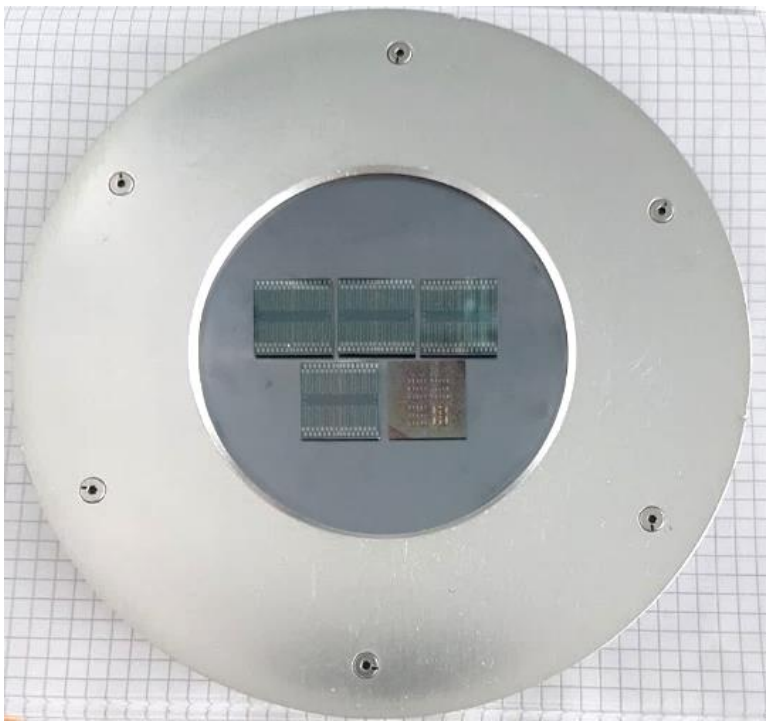

*Figure 11: Samples mounted on substrate holder for Ar ion etching.*

## 2.4. Assemby of Silicon Based CuO Thin Film Gas Sensors

In order to detect gases with CuO thin films, elevated temperatures are necessary. For this the structured CuO films on the FunkyNano platform chips were employed and assembled in a specific setup to provide heating up to 400 °C. First, the 2 x 2 $cm^2$ samples were cleaved in smaller pieces, next the samples were glued on a Si-substrate, where two Pt microheaters (10x2 Pt 6.8-0.4, Delta-R GmbH) and a Pt thermocouple (10x2.0 Pt 100 B, Delta-R GmbH) were integrated. This is a standard assembly developed at MCL for fast realization of prototype gas sensor devices. This setup is designed to fit into the gas measurement chamber and enables characterization of the gas sensor device. The support material consists of a bare Si substrate. Two platinum heaters and a thermocouple were glued onto the Si substrate with help of a high thermal conductive adhesive (Ceramabond 865; T-E-Klebetechnik). In order to increase the viscosity of the adhesive, a thinner (865-T, T-E-Klebetechnik) was used. The upper part of the sensor consists of the nanostructured silicon based CuO sample, which was also glued on. The wires of the microheaters and the thermocouple were soldered onto a custom-made printed circuit board (PCB; LxWxH 4.4x3.0x0.8 mm; designed by MCL and fabricated by mb-Technologies GmbH). With this assembly, mechanical support, electrical connection and thermal insulation in the measurement chamber were provided. The electrodes on the Si substrate were wire bonded to the carrier pads via gold wires with a thickness of 70 µm. Therefore, a wire bonder (F & K DELVOTEC Bondtechnik GmbH, type 5330) was used at AIT. Figure 12 shows the final assembled gas sensor stack.

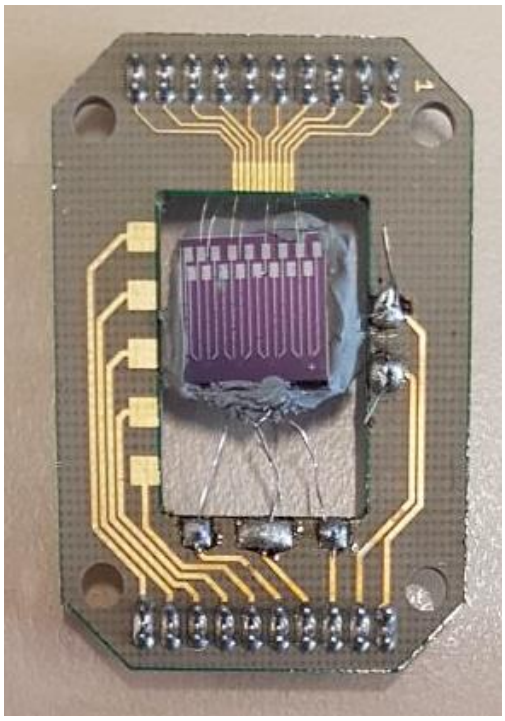

*Figure 12: CuO based gas sensor.*

# 3. Thin Film Characterization

In order to characterize thin film properties, samples were systematically investigated by various analytical techniques. These included optical microscopy, scanning electron microscopy (SEM), atomic force microscopy (AFM), x-ray diffraction (XRD) and Raman spectroscopy. In the following chapter, the used systems and devices are named and results of element as well as structural and surface analysis are presented. XRD and Raman plots as well as microscope images are discussed; structural properties, topography and film thickness are investigated. Furthermore, the effects of precursor solution concentration on the thin film properties are discussed.

## 3.1. Element Analysis

According to Abdelmounaïm et al. [25], structural properties of copper oxide thin films deposited by spray pyrolysis are affected by the precursor solution concentration. The authors show that, depending on the precursor concentration, not only CuO (tenorite) but also $Cu_2O$ (cuprite) is deposited. In case of 0.05 and 0.1 M precursor solution, thin films show a single phase CuO. In case of 0.2 and 0.3 M precursor solution, a mixed phase of CuO and $Cu_2O$ is obtained.

In this thesis, single phase CuO as p-type semiconductor material for the fabrication of MOS gas sensors was desired. For phase determination, the fabricated thin films were characterized by XRD and Raman spectroscopy. The XRD analysis were conducted using a diffractometer (Bruker D8 Discover with Eulerwiege) operating with CuK α radiation (λ = 1.54 Å) and θ - 2θ scan in parallel beam geometry. Tube voltage was 37 kV and tube current was 32 mA. EVA software (Bruker AXS) was used for phase determination. Raman spectroscopy was carried out on a Horiba Jobin-Yvon LabRAM HR800 UV-vis μ-Raman spectroscope with a green laser at a wavelength of 532.2 nm.

Figure 13 shows XRD patterns of CuO thin films deposited for 12 min with 0.1 M $CuNit_2$ (red), 0.1 M $CuCl_2$ (blue) and 0.1 M $CuAc_2$ (green) precursor solution. The patterns show 10 peaks at equal positions with similar intensities. The high intensity peak at 2Θ position 52 - 53° can be assigned to reflexes of the Si substrate. These reflexes are visible due to secondary excitations in the Si substrate influenced by the incidence angle.

Nine peaks observed at 2Θ positions 32.53, 35.56, 38.75, 48.75, 53.50, 58.36, 61.57, 66.28 and 68.14 are assigned to the crystal planes of (110), (-111), (111), (-202), (020), (202), (-113), (-311) and (220), respectively of CuO phase. This peak assignment was made by comparing the experimental data with the standard ICDD pattern (Card # 01-073-6023) for CuO.

No additional peak is observed other than Si (substrate) or CuO. Thus, XRD analysis proofs the existence of single phase CuO, deposited with 0.1 M precursor solution $CuNit_2$, $CuCl_2$ and $CuAc_2$.

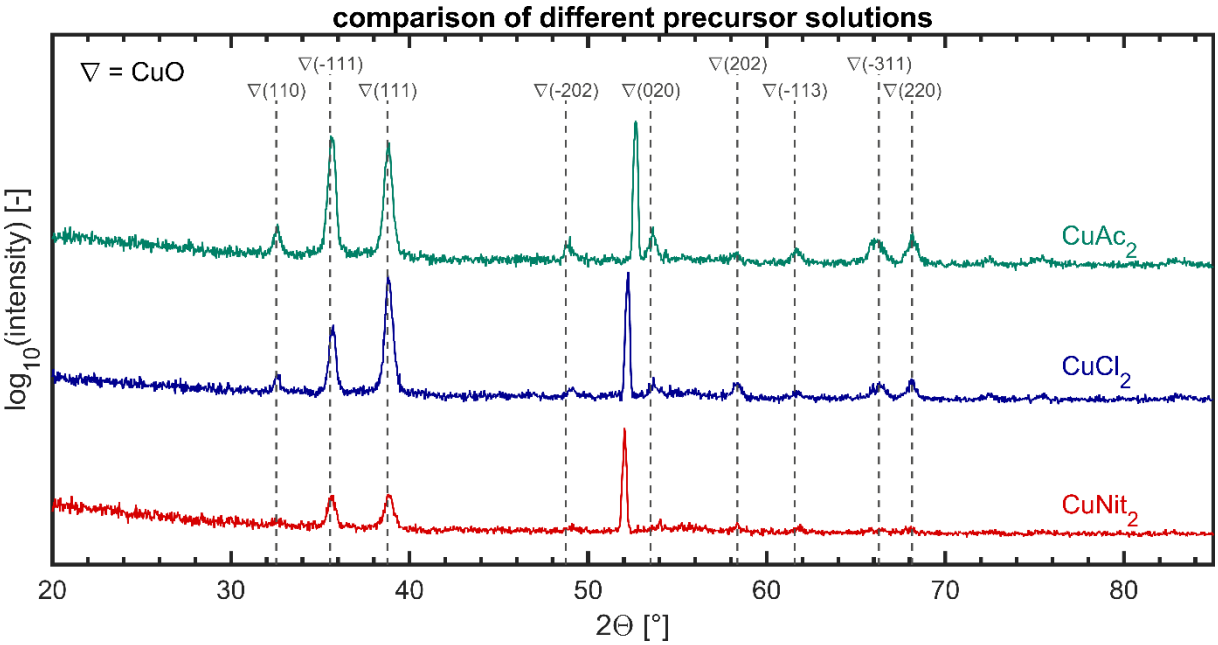


*Figure 13: XRD patterns of CuO thin films deposited for 12 min with 0.1 M $CuNit_2$ (red), 0.1 M $CuCl_2$ (blue) and 0.1 M $CuAc_2$ (green) precursor solutions.*

Figure 14, Figure 15 and Figure 16 show the XRD patterns of CuO thin films deposited for 7 min with $CuNit_2$, $CuCl_2$ and $CuAc_2$ precursor solution with different concentration, respectively. All patterns show equal peaks, independent from the precursor solution and their concentration. Peak intensity is similar for samples deposited with 0.1, 0.2 and 0.3 M precursor solutions. For samples deposited with 0.05 M precursor solution, peak intensity is lower, since less material was deposited. As a result of lower film thicknesses, lower peak intensities are obtained.

The peak at 2Θ position 52 - 53° can again be assigned to Si substrate reflexes. Except from the Si peak, all other peaks can be assigned to CuO, confirming the presence of single phase CuO. Consequently, the formation of mixed phase CuO and $Cu_2O$ can be ruled out and the independence of precursor concentration on phase formation can be assured.

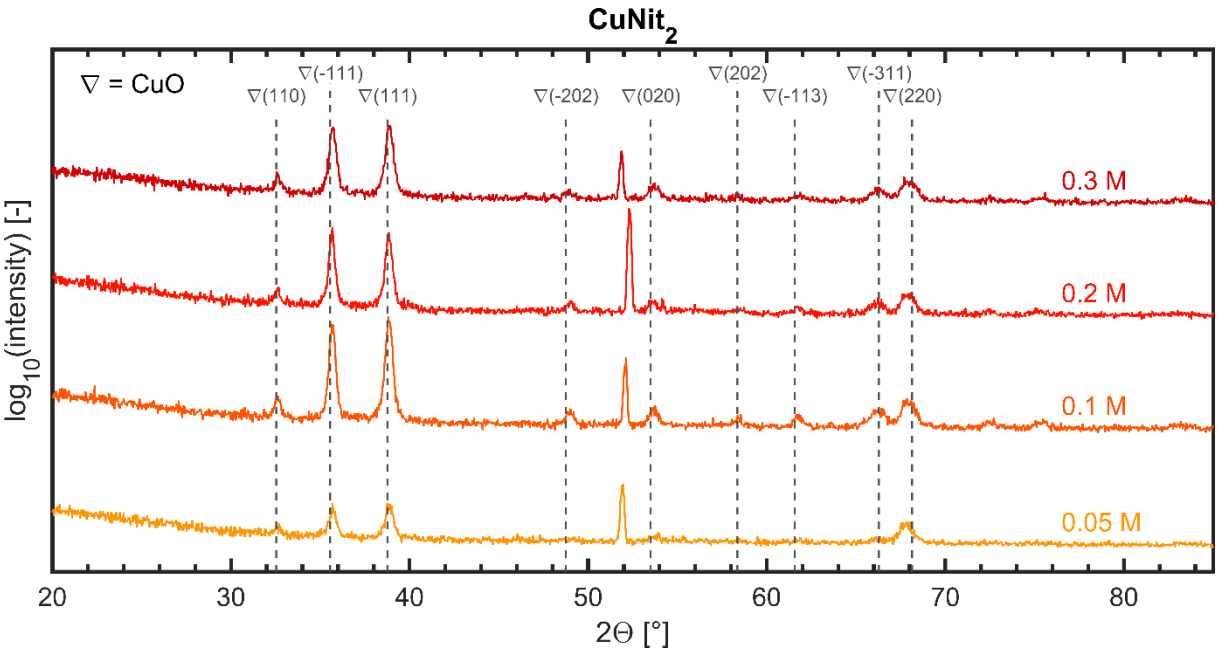


*Figure 14: XRD patterns of CuO thin films deposited for 7 min with differently concentrated $CuNit_2$ precursor solutions (0.05 M, 0.1 M, 0.2 M, 0.3 M).*

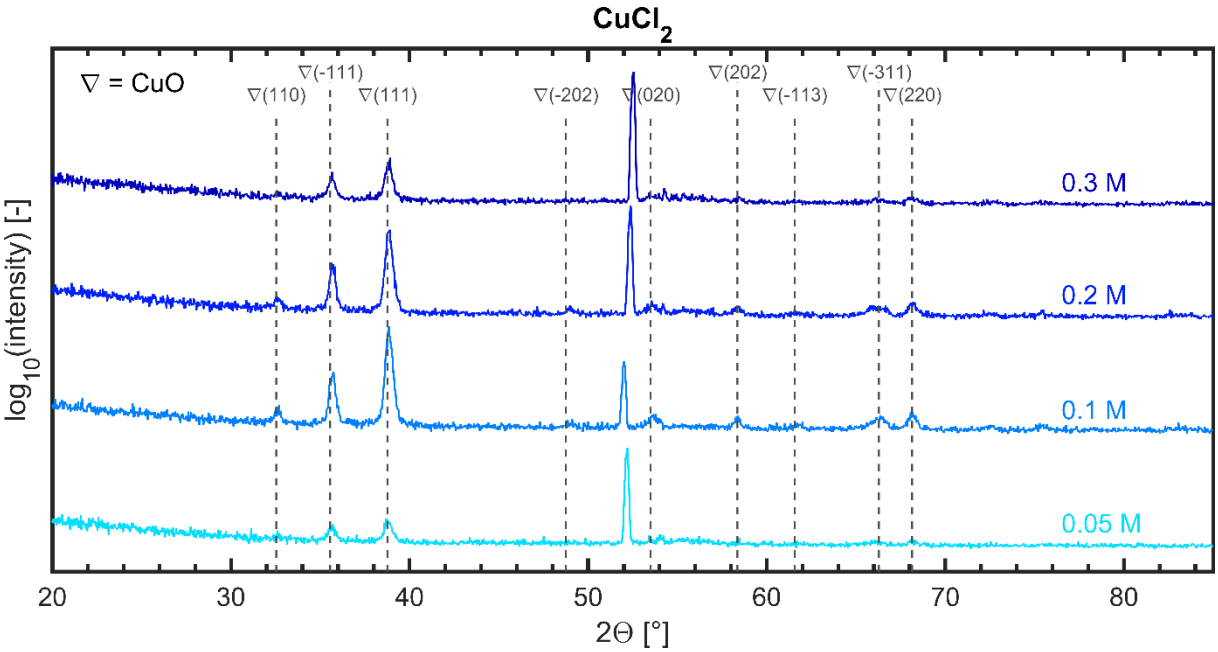


*Figure 15: XRD patterns of CuO thin films deposited for 7 min with differently concentrated $CuCl_2$ precursor solutions (0.05 M, 0.1 M, 0.2 M, 0.3 M).*

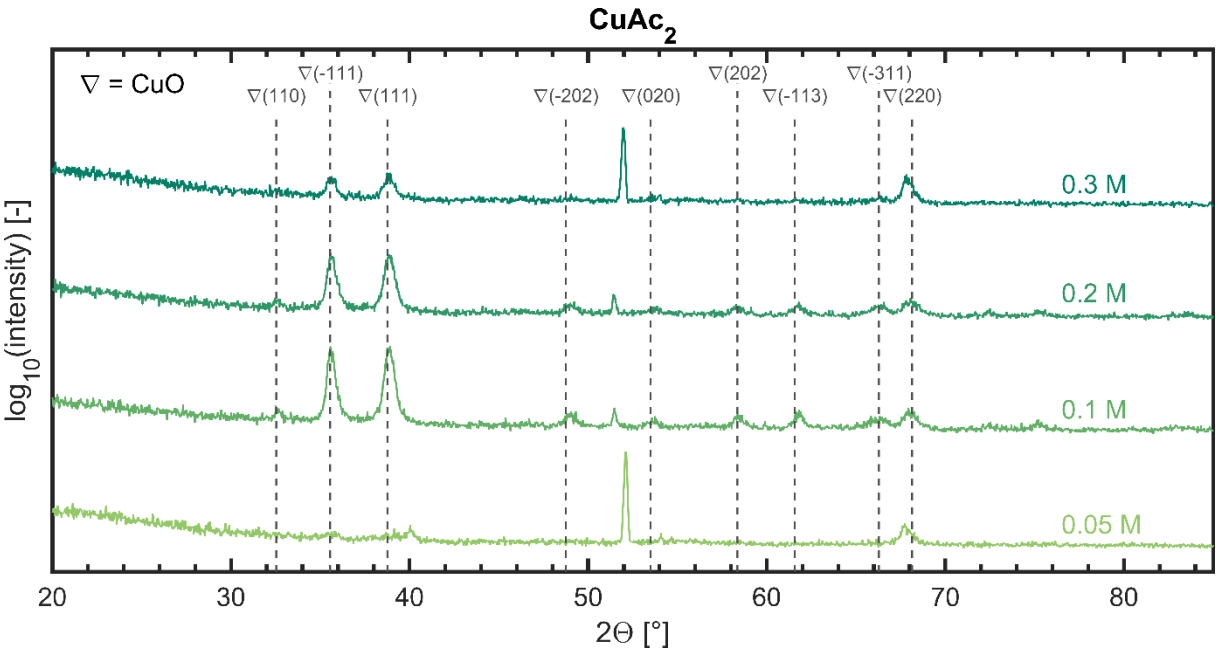


*Figure 16: XRD patterns of CuO thin films deposited for 7 min with differently concentrated $CuAc_2$ precursor solutions (0.05 M, 0.1 M, 0.2 M, 0.3 M).*

Raman spectroscopy is an analytical technique to determine the chemical composition of materials. In addition to XRD, it was used for phase determination of the deposited material.

According to Chrzanowski and Irwin [26], there are three room temperature Raman vibrational bands appearing at 298, 345 and 632 $cm^{-1}$ for CuO. These three peaks are clearly visible in the recorded Raman spectra of CuO thin films deposited for 10 min with 0.1 M $CuNit_2$ (red), 0.1 M $CuCl_2$ (blue) and 0.1 M $CuAc_2$ (green) precursor solution (Figure 17).

The peak at 522 $cm^{-1}$ can be assigned to the Si substrate. The characteristic peaks of $Cu_2O$, normally observed at 146, 219, 411 and 630 $cm^{-1}$ are not detected in the spectra [27].

Accordingly, peak assignment revealed the unexceptional presentence of single phase CuO. The film composition, namely single phase CuO, is therefore not only confirmed by XRD but also by Raman spectroscopy.

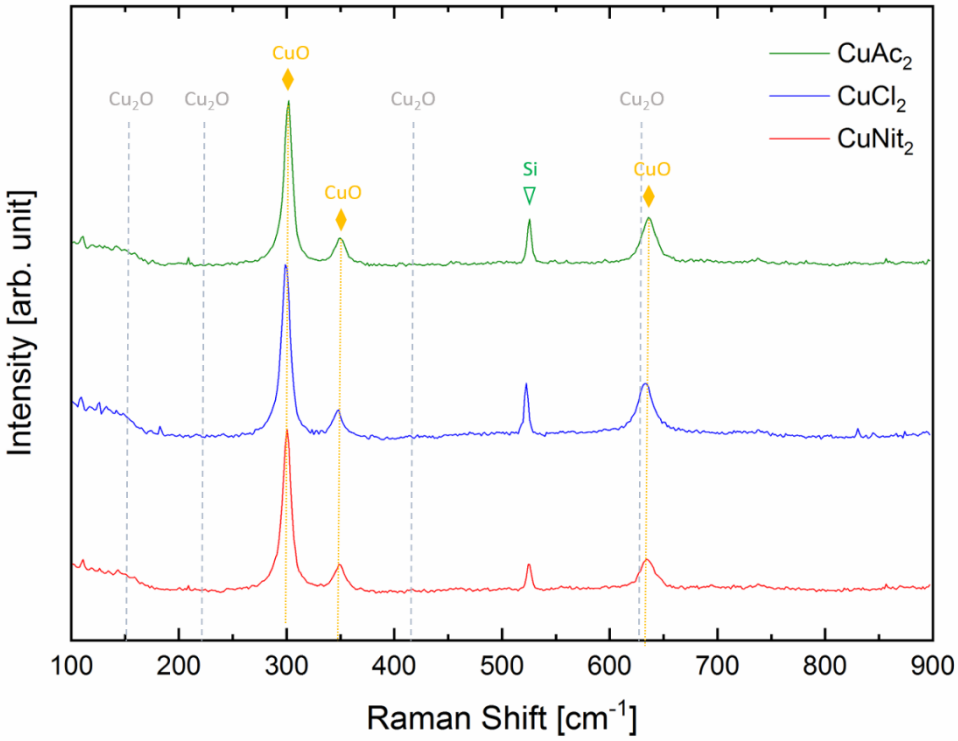


*Figure 17: Raman spectra of CuO thin films deposited for 10 min with 0.1 M $CuNit_2$ (red), 0.1 M $CuCl_2$ (blue) and 0.1 M $CuAc_2$ (green) precursor solutions.*

## 3.2. Copper Nitrate Precursor Solution

The first step in qualitative determination of structural properties was the investigation of thin films with an optical microscope (Zeiss Axio Scope.A1). The thin films were examined in different magnification levels (5x, 10x, 20x, 50x, 100x). Furthermore, the film thickness was determined with a coupled interferometer (Filmetrics F40 thin film analyzer).

CuO thin films fabricated with $CuNit_2$ precursor solution appeared as dark greyish layer evenly distributed over the substrate, which corresponds to uniform deposition. The layer thickness of films sprayed at 400 °C for 10 min was determined to range from 90 – 120 nm depending on the used precursor concentration. The use of 0.1 M precursor solution, formed films of 100 nm thickness.

Figure 18 shows optical microscope images of CuO thin films deposited for 12 min with 0.1 M $CuNit_2$ precursor solution. Image a), b) and c) show bright field images in different magnifications; image d), e) and f) show dark field images in different magnifications. The images show a continuous film with lots of small crystallites. These speckles can be assigned to CuO agglomerates in the form of elevations on the thin film. The thin film surface seems to be rough and characterized by numerous CuO agglomerates.

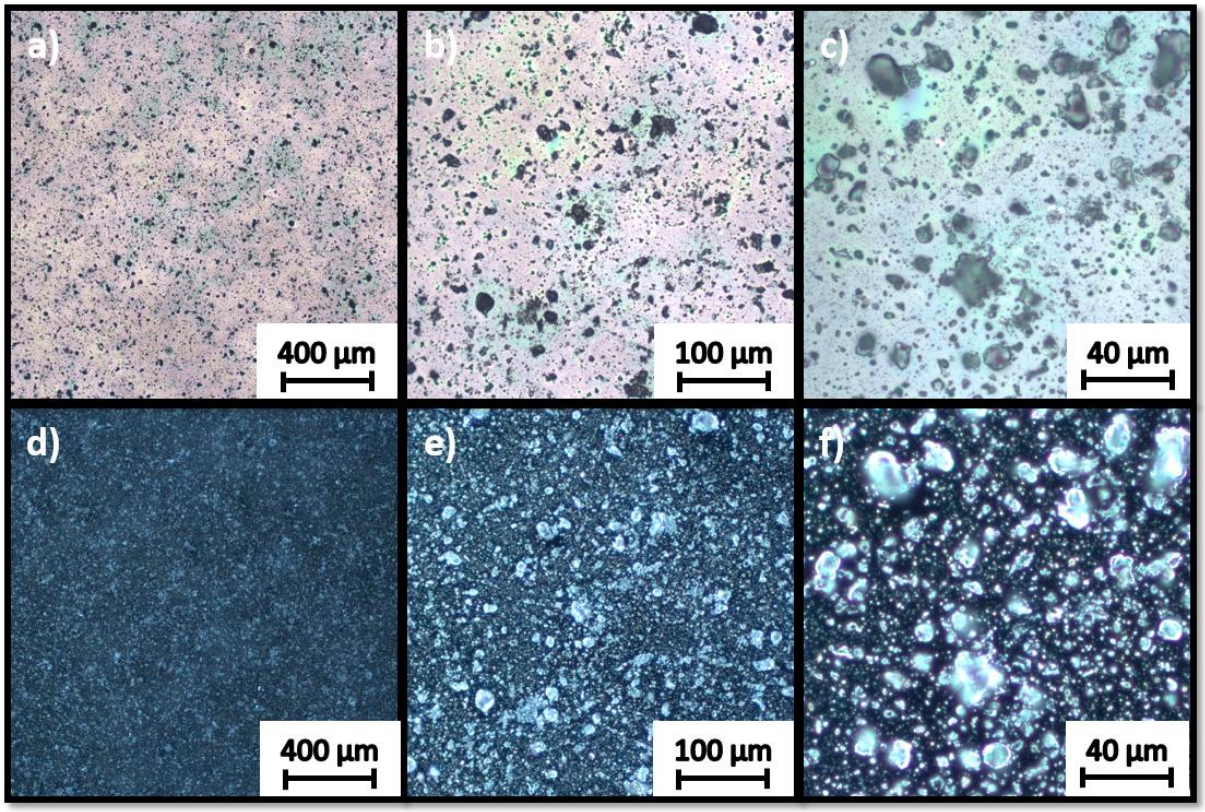


*Figure 18: Microscope images of CuO thin films deposited with 0.1 M $CuNit_2$ precursor solution for 12 min; a-c): bright field images in different magnifications; d-f) dark field images in different magnifications.*

Giving a detailed insight into the thin film surface characteristics, a high-resolution scanning electron microscope (SEM) was used (Zeiss Crossbeam 340). Figure 19, Figure 20 and Figure 21 show SEM images of CuO thin films deposited for 10 min with 0.1 M $CuNit_2$ precursor solution in different magnifications. The films are characterized by a dense structure with differently sized particle accumulations on the surface. µ-Raman measurements of those particles revealed that their chemical composition represents the film composition as CuO.

Some of the surface features are burst-like. These structures could be the result of the evaporation of volatile residues within the growing film. Interestingly, these burst-like features are only found for films grown with $CuNit_2$, but not for $CuCl_2$ or $CuAc_2$. Figure 21 shows the highest investigated magnification. Only this magnification yields insight into the sub-micron surface features, namely a granular, dense surface of facetted crystals.

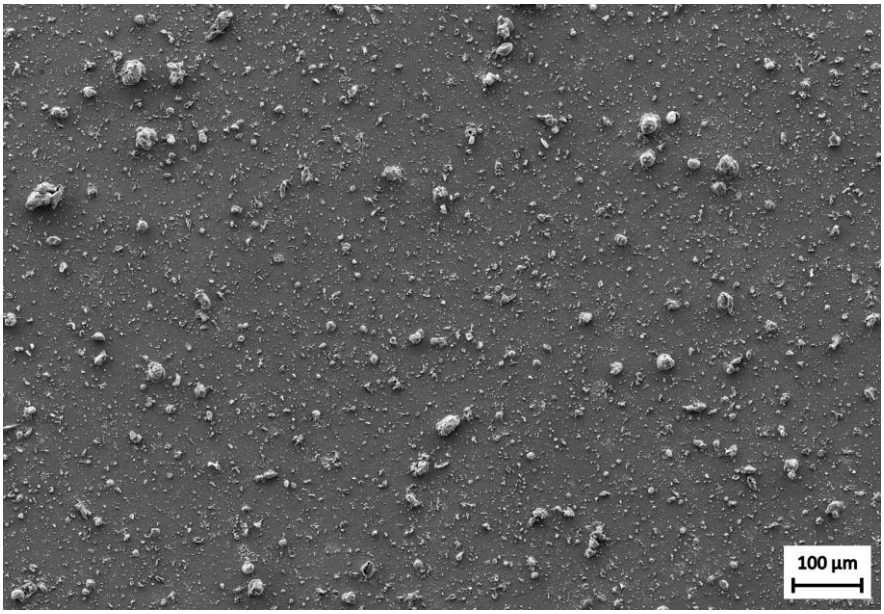


*Figure 19: SEM image of CuO thin film deposited with 0.1 M $CuNit_2$ precursor solution for 10 min.*

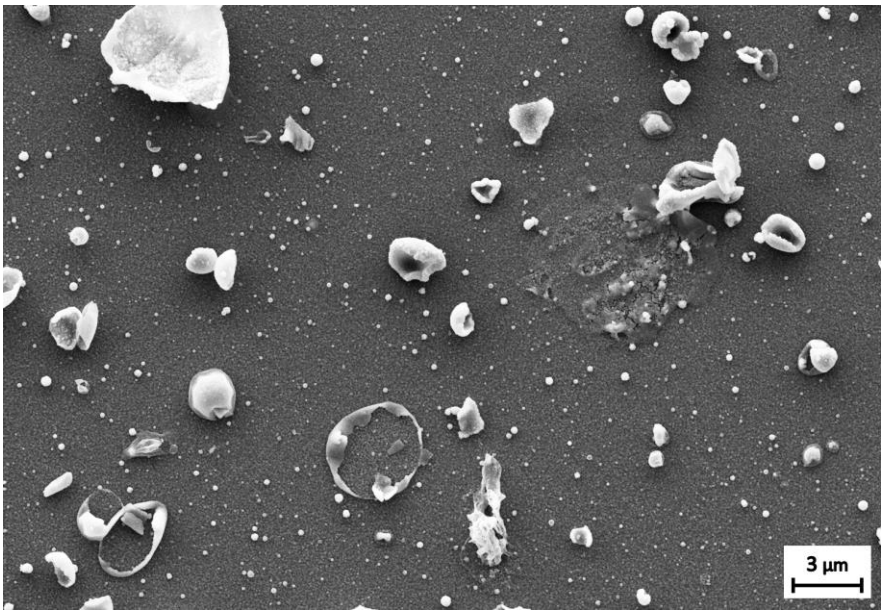


*Figure 20: SEM image of CuO thin film deposited with 0.1 M $CuNit_2$ precursor solution for 10 min.*

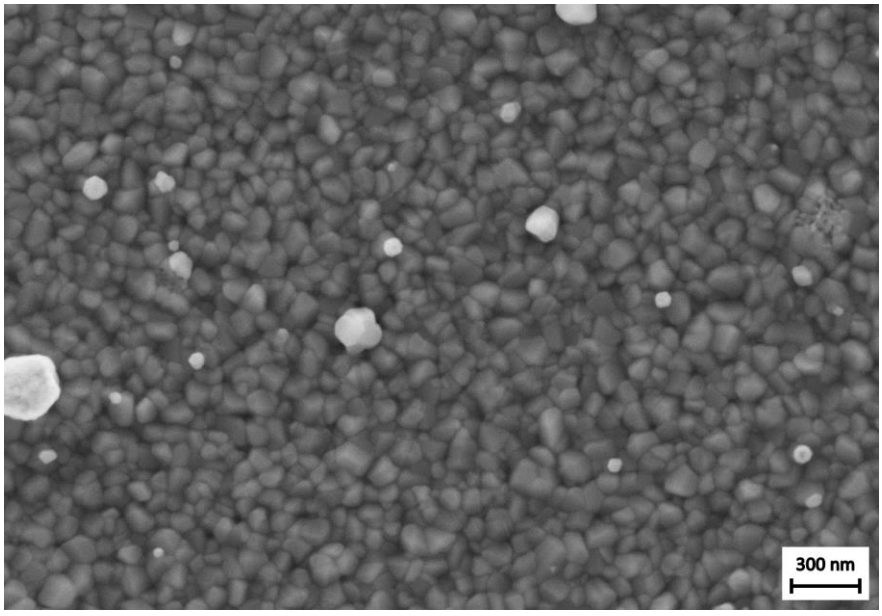


*Figure 21: SEM image of CuO thin film deposited with 0.1 M $CuNit_2$ precursor solution for 10 min.*

In order to analyze the topography and layer thickness of thin films, an atomic force microscope (DME-AFM with option for FE-SEM; Model Nr.: 2770; Danish Micro Engineering) was used. Figure 22 shows the topography of a CuO thin film deposited for 10 min with 0.1 M $CuNit_2$ precursor solution. In this figure, the granular surface of the CuO thin film is evident. The single grains are closely packed and differently sized. The determined average thin film roughness is 8.5 nm, which is higher than for films deposited with $CuAc_2$ but lower than for film deposited with $CuCl_2$. The root mean square roughness yields 11.0 nm.

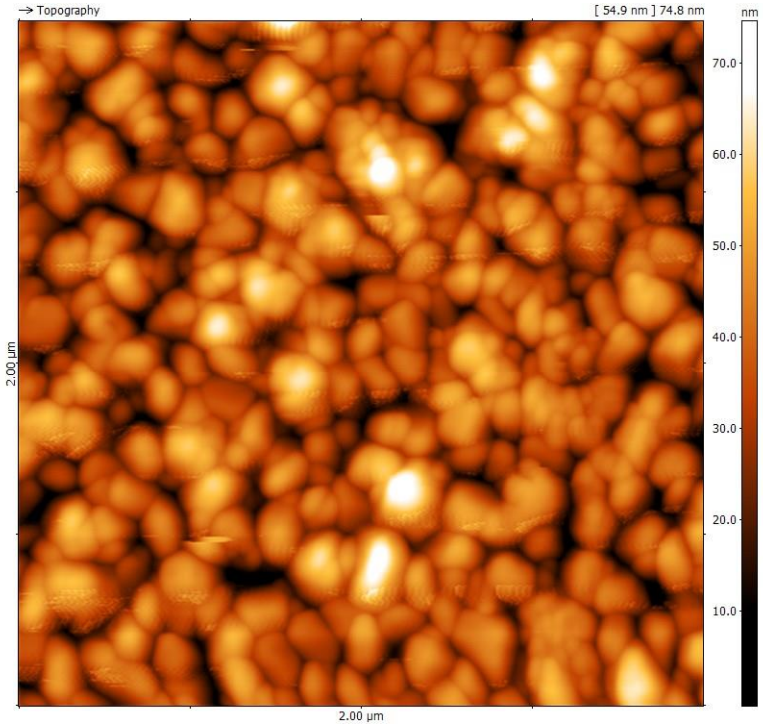


*Figure 22: AFM image of CuO thin film deposited with 0.1 M $CuNit_2$ precursor solution for 10 min.*

## 3.3. Copper Chloride Precursor Solution

The $CuCl_2$ precursor yields a dark greyish CuO thin film similar to those obtained by $CuNit_2$ precursor solution. Generally, deposition with $CuCl_2$ precursor solution was faster and yielded thicker layers than with other precursors. In case of 0.1 M precursor solution, film thicknesses of roughly 150 nm were determined.

Figure 23 shows optical microscope images of CuO thin films deposited for 12 min with 0.1 M $CuCl_2$ precursor solution. Image a), b) and c) show bright field images in different magnifications, whilst image d), e) and f) show dark field images in different magnifications. These images show CuO thin films characterized by diverging layer thicknesses and many CuO agglomerates. However, less CuO agglomerates than on films fabricated with $CuNit_2$ precursor solution were observed.

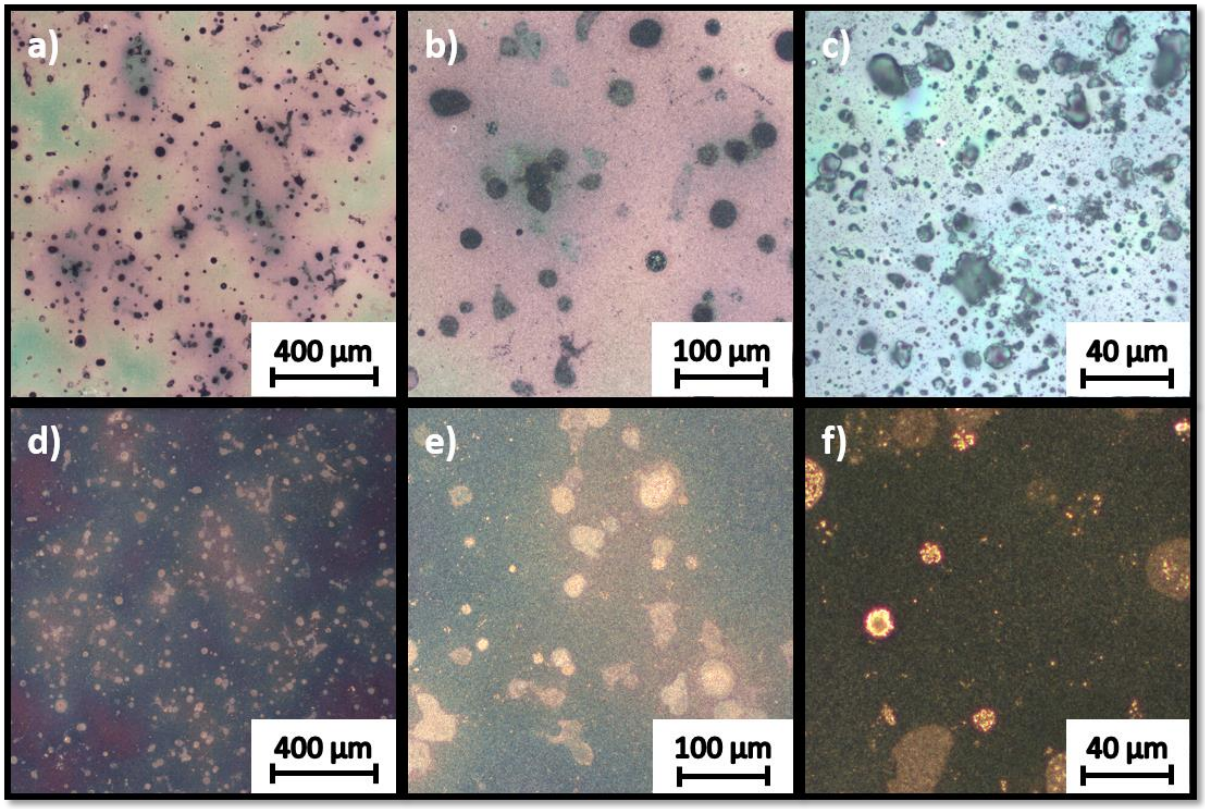


*Figure 23: Microscope images of CuO thin films deposited with 0.1 M $CuCl_2$ precursor solution for 12 min; a-c): bright field images in different magnifications; d-f) dark field images in different magnifications.*

Figure 24, Figure 25 and Figure 26 show SEM images of CuO thin films deposited for 10 min with 0.1 M $CuCl_2$ precursor solution. In contrast to films deposited with $CuNit_2$ and $CuAc_2$ precursors, films deposited with $CuCl_2$ features a completely different surface morphology.

Bright areas in Figure 24 and Figure 25 can be assigned to circular arranged particle accumulations. Moreover, some large isolated particles stick to the rather rough surface. Figure 26 yields a detailed insight into the sub-micron surface features, namely needle-like, angular crystals which are randomly arranged.

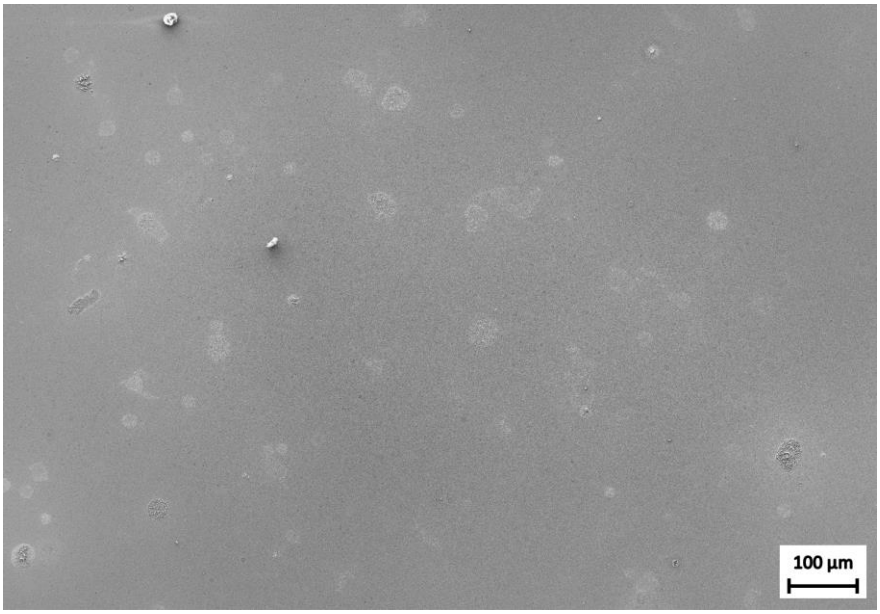


*Figure 24: SEM image of CuO thin film deposited with 0.1 M $CuCl_2$ precursor solution for 10 min.*

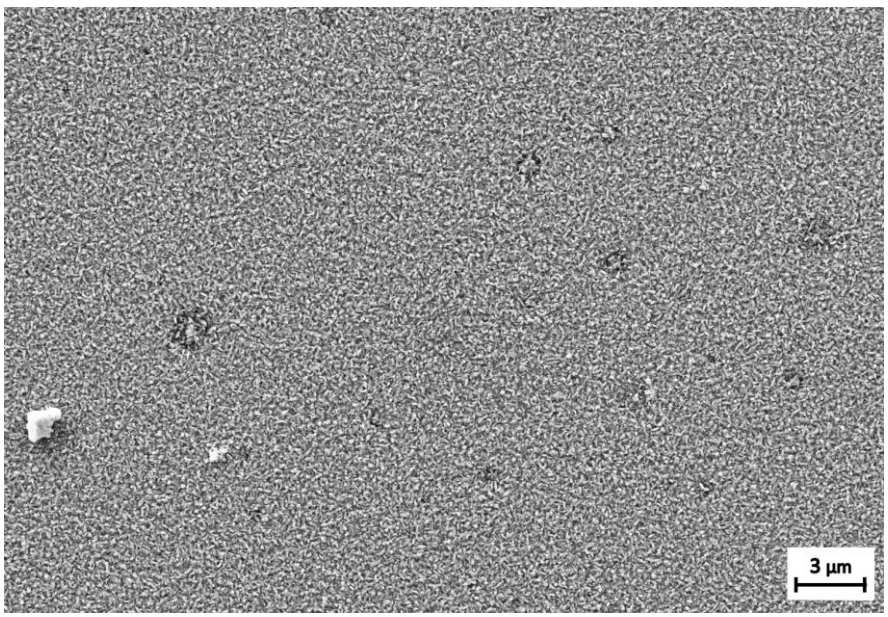


*Figure 25: SEM image of CuO thin film deposited with 0.1 M $CuCl_2$ precursor solution for 10 min.*

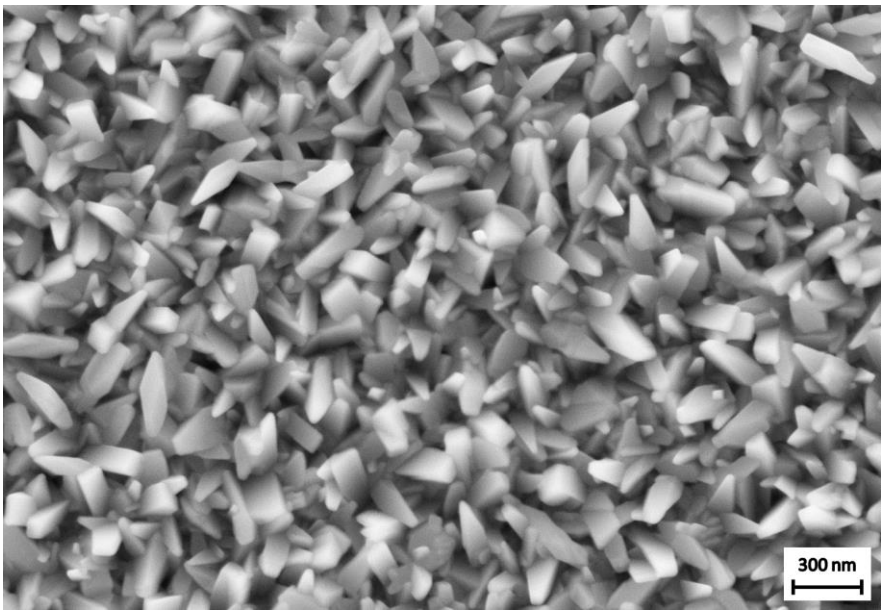


*Figure 26: SEM image of CuO thin film deposited with 0.1 M $CuCl_2$ precursor solution for 10 min.*

AFM analysis confirms the needle-like surface morphology observed with SEM. The thin film surface is characterized by closely spaced angular crystals, resulting in a rough topography. Determination of the average roughness exhibits a value of 22.0 nm; the root mean square roughness yields 27.0 nm. Accordingly, $CuCl_2$ yields the roughest thin films, compared to other precursors.

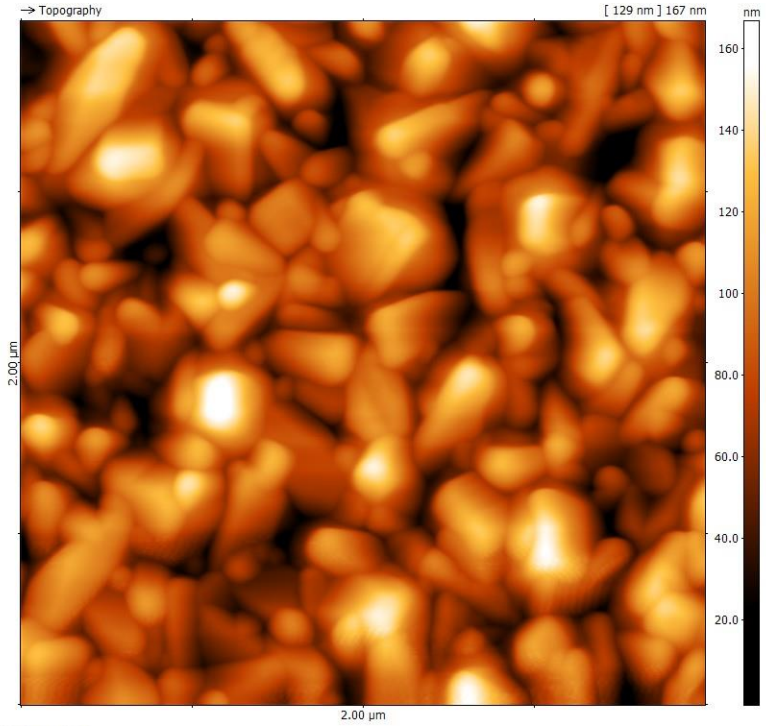


*Figure 27: AFM image of CuO thin film deposited with 0.1 M $CuCl_2$ precursor solution for 10 min.*

## 3.4. Copper Acetate Precursor Solution

The $CuAc_2$ precursor solution yields sprinkled yellow CuO thin films (Figure 28), in contrast to dark greyish layers obtained with $CuNit_2$ and $CuCl_2$. Red crystallites are randomly distributed on the yellow CuO thin film, which were assigned to CuO islands. Moreover, the direction of the spray beam can be observed. While showing high deposition at the bottom (dark yellow) of the sample, less CuO has been deposited in the upper blueish part. The determined thickness of CuO thin films fabricated with 0.1 M $CuAc_2$ precursor solution at a spray time of 10 min is roughly 70 nm.

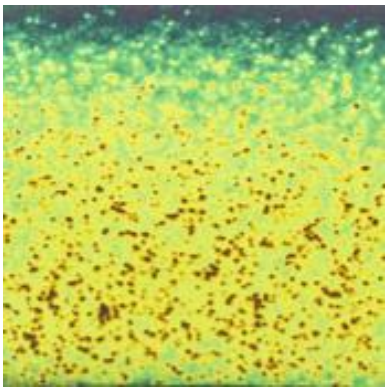

*Figure 28: 2x2 cm Si substrate covered by a CuO thin film deposited with 0.1 M $CuAc_2$ precursor solution for 12 min.*

Figure 29 shows microscope images of CuO thin films deposited for 12 min with 0.1 M $CuAc_2$ precursor solution. Image a), b) and c) show bright field images in different magnifications; image d), e) and f) show dark field images in different magnifications. The violet areas in image a) and b) correspond to thicker CuO films, which are visible to the naked eye in Figure 28 as red crystallites. It seems like the thin film thickness is inhomogeneous and more CuO has been deposited at specific positions. In comparison to other precursors, $CuAc_2$ yields the lowest number of CuO agglomerates.

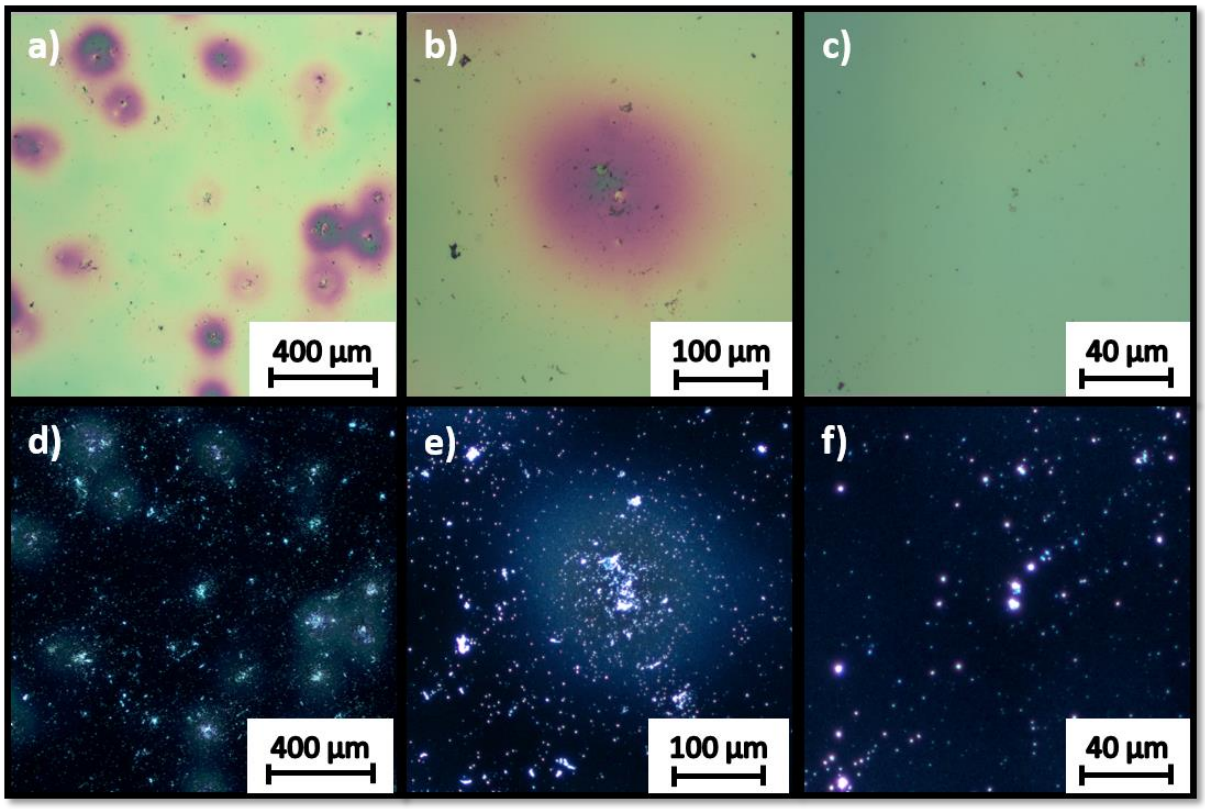


*Figure 29: Optical microscope images of CuO thin films deposited with 0.1 M $CuAc_2$ precursor solution for 12 min; a-c): bright field images in different magnifications; d-f) dark field images in different magnifications.*

Figure 30, Figure 31 and Figure 32 show SEM images of CuO thin films deposited for 10 min with 0.1 M $CuAc_2$ precursor solution. Figure 30 shows a few large particles sticking to an otherwise dense film. Figure 31 and Figure 32 instead show fine isolated grains evenly distributed over the whole area.

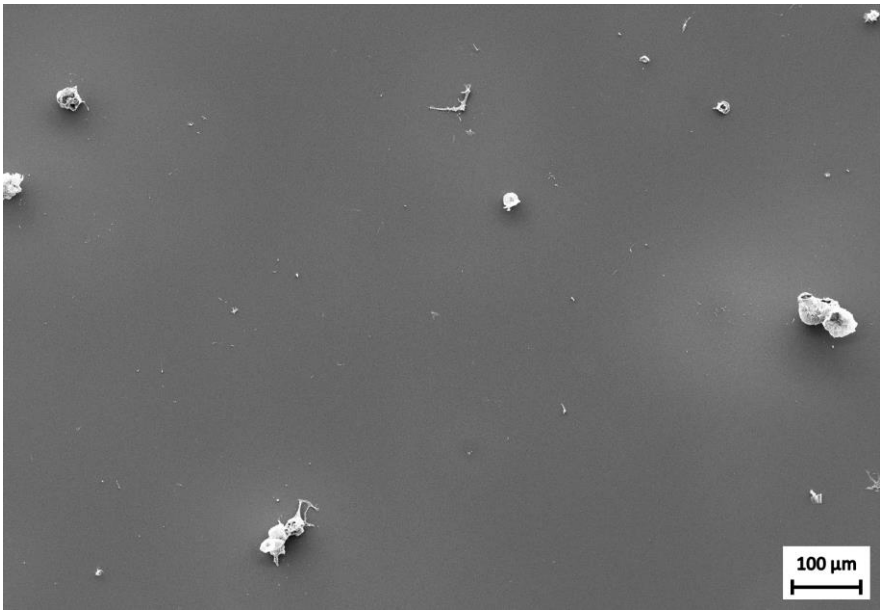


*Figure 30: SEM image of CuO thin film deposited with 0.1 M $CuAc_2$ precursor solution for 10 min.*

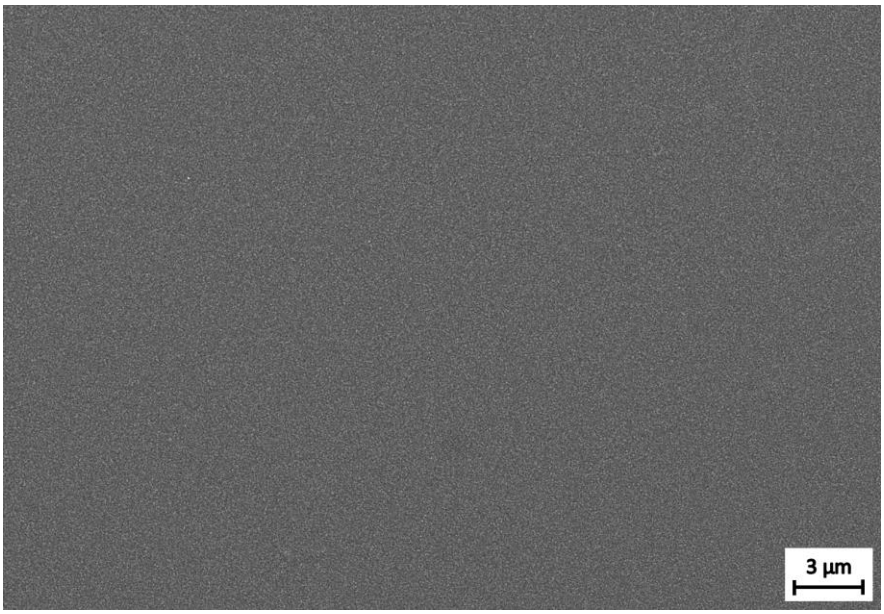


*Figure 31: SEM image of CuO thin film deposited with 0.1 M $CuAc_2$ precursor solution for 10 min.*

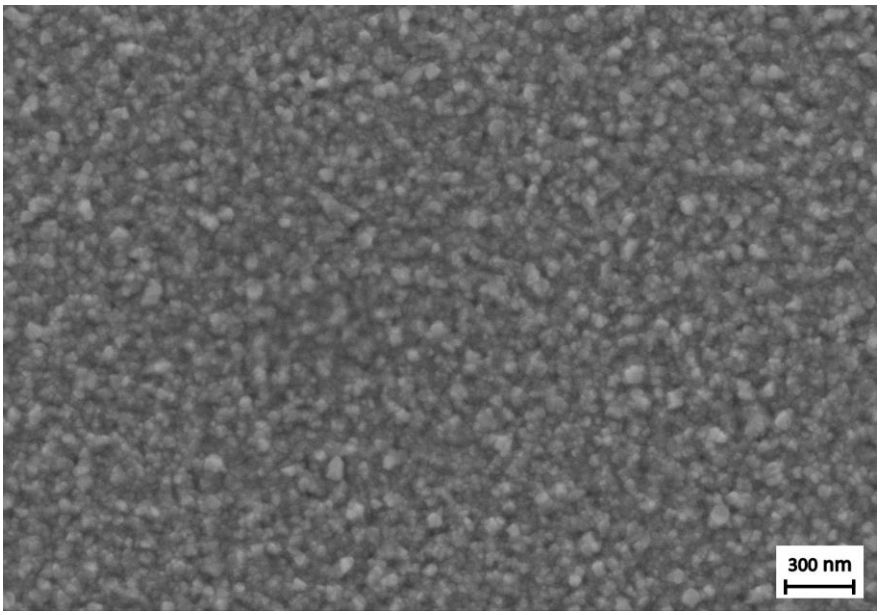


*Figure 32: SEM image of CuO thin film deposited with 0.1 M $CuAc_2$ precursor solution for 10 min.*

AFM analysis allows to obtain further insights into the CuO surface topography. Figure 33 shows fine, granular crystals distributed over the thin film surface. Besides granular surface features, a low film roughness average of 4.2 nm and a root mean square roughness of 5.2 nm was determined. When comparing the thin film roughness properties, the smoothest films were obtained with the $CuAc_2$ precursor.

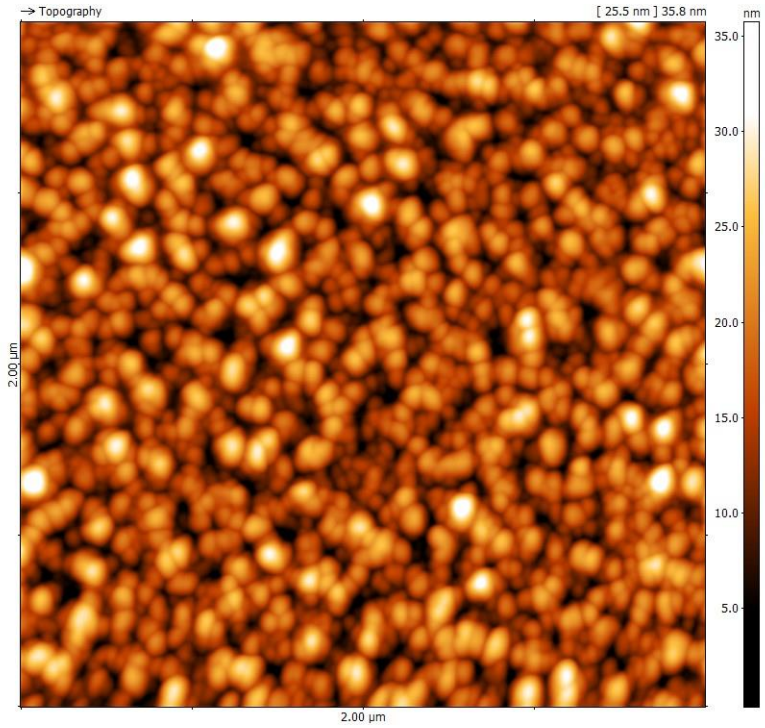


*Figure 33: AFM image of CuO thin film deposited with 0.1 M $CuAc_2$ precursor solution for 10 min.*

## 3.5. Summary of Thin Film Characterization

Table 5 gives an overview of the qualitative and quantitative thin film properties. The characterized thin films were deposited with 0.1 M $CuNit_2$, $CuCl_2$ and $CuAc_2$ precursor solution; spray time was 10 min. Comparing the thin films obtained with different precursors, $CuAc_2$ shows the lowest film thickness, the lowest amount of CuO islands, the lowest deposition rate and the lowest film roughness. $CuCl_2$ instead yields the thickest films with many CuO islands, high deposition rate and high film roughness. $CuNit_2$ can be found in-between, yielding 100 nm thick films with many CuO islands, medium deposition rate and film roughness.

*Table 5: Qualitative and quantitative description of CuO thin films sprayed with 0.1 M precursor solution for 10 min.*

| **Precursor** | **Qualitative description** | **Thickness [nm]** | **Deposition Rate [nm/min]** | **Roughness average [nm]** | **Root mean square roughness [nm]** |
|---|---|---|---|---|---|
| **$CuNit_2$** | Many CuO islands | 100 | 10 | 8.5 | 11.0 |
| **$CuCl_2$** | Many CuO islands | 150 | 15 | 22.0 | 27.0 |
| **$CuAc_2$** | Few CuO islands | 70 | 7 | 4.2 | 5.2 |

Based on these experimental results, $CuAc_2$ was preferably used as precursor for the deposition of CuO thin films.

# 4. Gas Measurements

## 4.1. Gas Measurement Setup

The sensitivity of the fabricated CuO thin films towards $CO_2$ and CO were tested in the gas measurement set up (Figure 34) consisting of:

- A gas measurement chamber,
- mass flow controllers (MFC, F-201CV from Bronkhorst) to regulate the gas supply,
- a current source to apply the required current to the heater (PL330P, from Thurlby Thandar Instruments)
- a source measure unit (2400 SourceMeter, from Keithley) to perform the resistance measurement of the sensor material,
- and a multimeter (34401A, from Agilent Technologies) to read out the sensor's thermocouple.

The used background gas was synthetic air (80% nitrogen, 20% oxygen from Linde Gas GmbH). The background gas flow was controlled by two MFCs: one gas stream was bubbled through a water reservoir to provide humidity, the other one represented the dry background gas flow. The relative humidity in the background gas flow was measured by a commercial humidity sensor (rh sensor, AFK-E from Kobold). The target gas flow was controlled by three MFCs. All MFCs were controlled by a computer using a LabView application. The total gas flow (background gas flow + target gas flow) fed to the gas chamber was kept constant at 1000 sccm for all gas measurements presented in this work.


*Figure 34: Gas measurement set up in the MCL laboratory.*

## 4.2. Resistance Measurements

The CuO thin film in the investigated gas sensor was deposited for 10 min via 0.3 M $CuAc_2$ precursor solution at a hotplate temperature of 400 °C. The gas sensing properties of the fabricated sensor were characterized upon the exposure to $CO_2$ and CO in the gas measurement set up. The sensor was exposed to various ppm-levels of $CO_2$ (500, 1000, 1500 and 2000 ppm) at three relative humidity (rH) levels (25, 50 and 75 %) and three different operating temperatures (300, 350 and 400 °C). Additionally, the same sensor was exposed to CO gas pulses of a volumetric fraction of 10, 50, 100 and 200 ppm at equal relative humidity levels and equal operating temperatures (graphs not shown in this thesis).

Figure 35, Figure 36 and Figure 37 show the sensor resistance (green) under exposure to different concentrations of $CO_2$ (dark grey) over the time (black) at relative humidity levels of 50, 25 and 75 % (blue) and a fixed operating temperature (either 300, 350 or 400 °C in red). The previously named figures are discussed in the following.

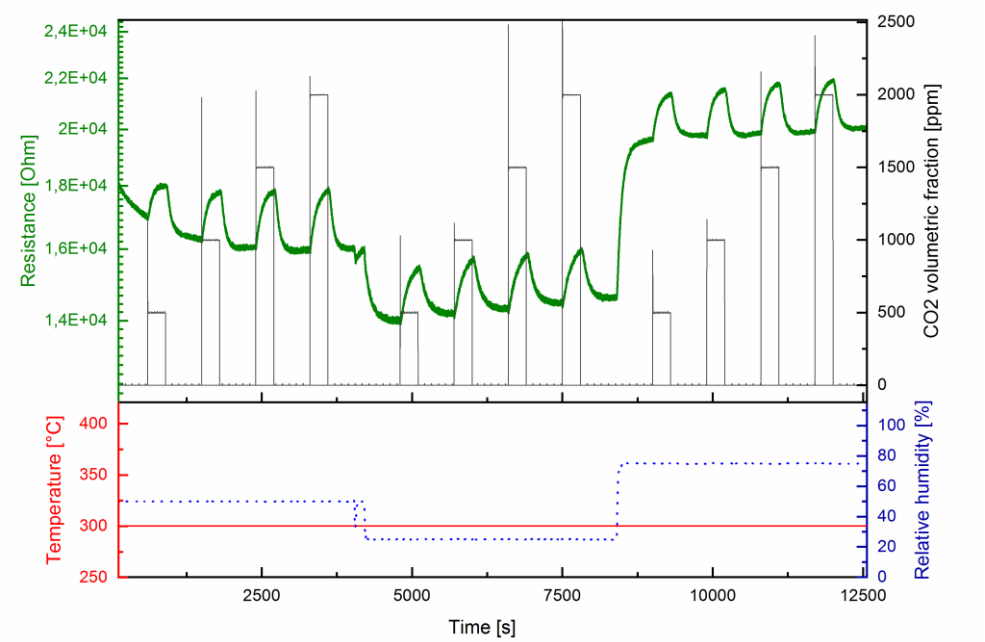


*Figure 35: Sensor resistance (green) responding to $CO_2$ pulses (500, 1000, 1500 and 2000 ppm) over the time (black) at different relative humidity levels (50, 25 and 75 % in blue) and a temperature of 300°C (red).*

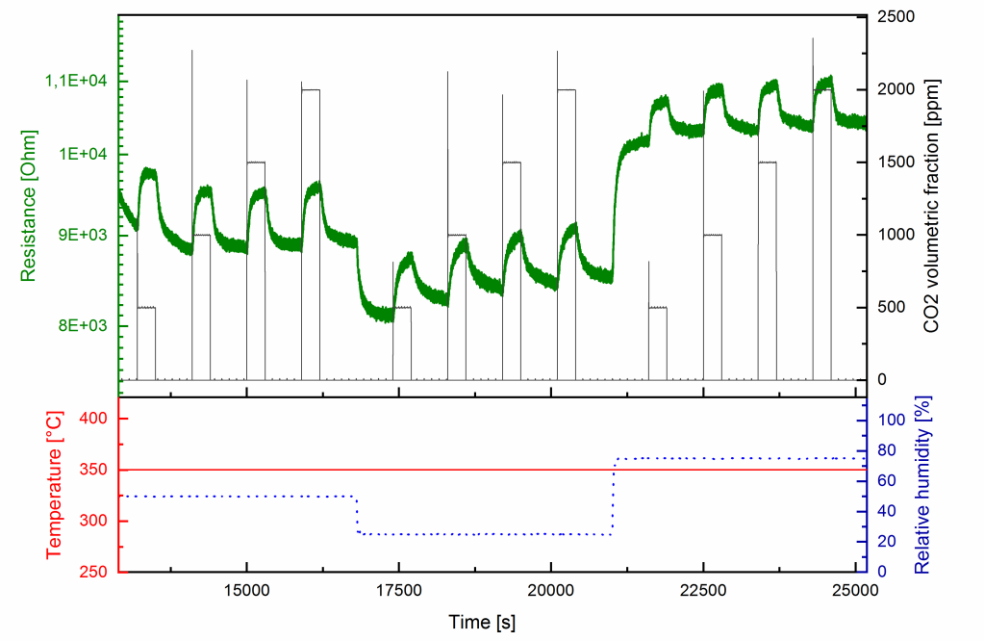


*Figure 36: Sensor resistance (green) responding to $CO_2$ pulses (500, 1000, 1500 and 2000 ppm) over the time (black) at different relative humidity levels (50, 25 and 75 % in blue) and a temperature of 350°C (red).*

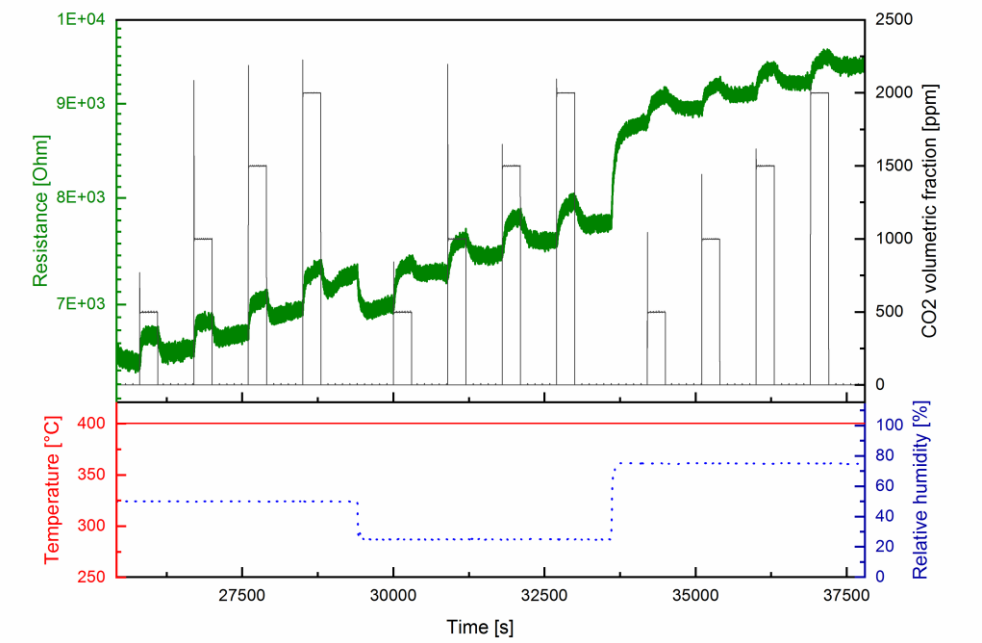


*Figure 37: Sensor resistance (green) responding to $CO_2$ pulses (500, 1000, 1500 and 2000 ppm) over the time (black) at different relative humidity levels (50, 25 and 75 % in blue) and a temperature of 400°C (red).*

Generally, sensor resistance varies between 6 – 22 kOhms in the investigated temperature and relative humidity range under exposure to $CO_2$ gas pulses (Figure 35, Figure 36 and Figure 37). At the lowest investigated temperature (300 °C), the sensor shows a resistance in the range of 14 – 22 kOhms and a baseline resistance of 16 kOhms at 50 % rH. 350 °C yield resistance values between 8 – 11 kOhms and a baseline resistance of 9 kOhms at 50 % rH. 400 °C yield resistance values between 6 – 10 kOhms and a baseline resistance of roughly 7 kOhms at 50 % rH. The obtained resistances are summarized in Table 6.

*Table 6: Estimated resistances of investigated CuO sensor at different operating temperatures.*

| **Operating temperature [°C]** | **Lowest investigated resistance [kOhms]** | **Highest investigated resistance [kOhms]** | **Investigated baseline resistance at 50 % rH** |
|---|---|---|---|
| **300** | 14 | 22 | 16 |
| **350** | 8 | 11 | 9 |
| **400** | 6 | 10 | 7 |

As stated by Rydosz and Szkudlarek [28], 50 nm CuO thin films exhibit baseline resistances of 9 kOhms at 380 °C and 15 kOhms at 320 °C operating temperature and a relative humidity level of 50 % in air. Accordingly, the recorded baseline resistances highly correspond to those found in literature.

Considering resistance values in Table 6, the lowest sensor resistance is investigated at the highest operating temperature (400 °C). This can be explained by the increase in charge carrier density of semiconductors at higher temperatures, resulting in a conductivity increase. Conversely, resistivity decreases at higher temperatures.

The affinity to humidity is a well-known characteristic of MOS gas sensors and has to be taken into account during the execution of the experiments [29]. As shown in Figure 35 and Figure 36 the increase of relative humidity induces a resistance increase. Figure 37 instead reveals no obvious humidity related changes in resistance. However, it shows steadily increasing resistance over the time. This leads to the assumption that the measurement period was not long enough for stabilizing the sensor, resulting in unstable resistance.

While exposure to $CO_2$, resistance of the CuO sensor increases. However, the impact of gas exposure on the resistance is independent from the gas pulse concentration. This leads to the assumption that the sensor has already reached its saturation level at the lowest gas pulse concentration.

## 4.3. Sensitivity of Gas Sensors

In the following chapter, the terms “sensitivity” and “response” will be used synonymously. The sensitivity S of p-type MOS gas sensors is mathematically defined as

$$S\,[\%] = \left(\frac{R_{gas}}{R_0} - 1\right) * 100 \qquad \text{Eq. 10}$$

,where $R_0$ is the sensor resistance in synthetic air and $R_{gas}$ is the sensor resistance under the influence of a reducing gas. This formula produces reasonable values ranging from zero (corresponds to zero interaction) up to high positive values for strong interactions with reducing gas species.

According to Ahlers, Müller *et al. [30],* the response of MOS gas sensors increases up to a certain temperature $T_M$, where a sensitivity maximum occurs. This temperature depends both on the kind and on the concentration of target gas applied. At sensor operation temperatures higher than $T_M$, the response slowly drops again.

In case of the investigated CuO based gas sensor, the sensitivity is detected to be maximum at an operating temperature of 300°C, revealing values up to 12 % (Figure 38). At temperatures higher than 300 °C, the response decreases to maximum values of roughly 8 % for 350 °C (Figure 39) and 6 % for 400 °C (Figure 40). This temperature dependent sensor response is typically expected for CuO based gas sensors [30]. Accordingly, it is assumed that the operating temperature for the sensitivity maximum $T_M$ is reached at 300 °C. Temperatures higher than 300 °C lower the sensor response.

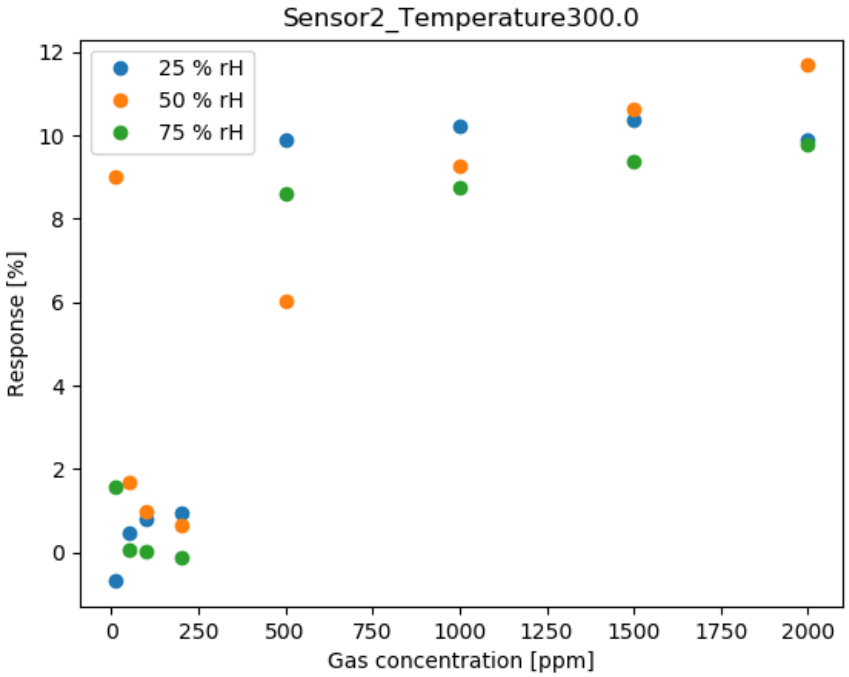


*Figure 38: Sensor response to CO (gas concentration < 250 ppm) and $CO_2$ (gas concentrations ≥ 500 ppm) at different levels of relative humidity (rH) at 300 °C.*

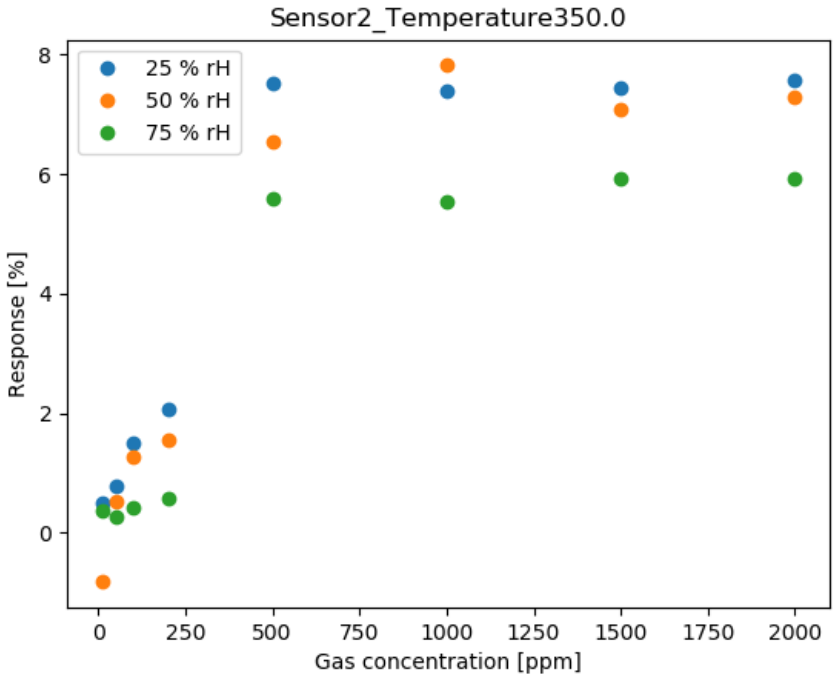


*Figure 39: Sensor response to CO (gas concentration < 250 ppm) and $CO_2$ (gas concentrations ≥ 500 ppm) at different levels of relative humidity (rH) at 350 °C.*

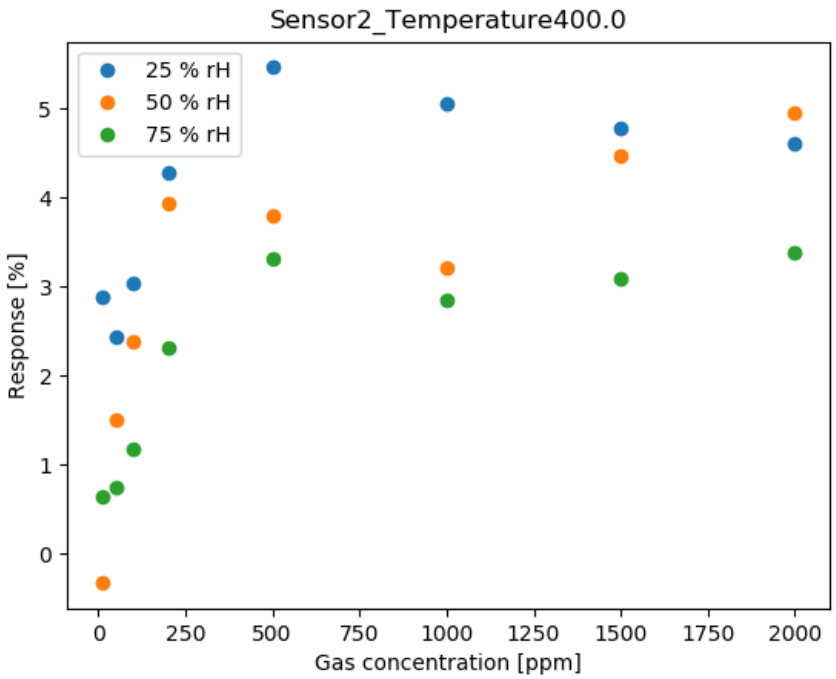


*Figure 40: Sensor response to CO (gas concentration < 250 ppm) and $CO_2$ (gas concentrations ≥ 500 ppm) at different levels of relative humidity (rH) at 400 °C.*

In terms of exposure to humidity, an obvious trend of lower sensitivity with increasing relative humidity comes clear. Besides a few exceptions, sensitivity is lowest at a relative humidity level of 75 %. This decrease in sensitivity at relative higher humidity levels can be attributed to the formation of water films on the MOS surface [31]. The water films decelerate the diffusion of $CO_2$ towards gas active centers, resulting in a sensitivity decrease.

Regarding the sensor sensitivity against various $CO_2$ concentrations, a trend of increasing sensitivity with increasing gas concentration would be assumed. However, no such linear trend between sensitivity and gas concentration can be observed, except for measurements conducted at 300 °C and 50 % relative humidity (orange dots at concentrations ≥ 500 ppm in Figure 38). Here, increase in $CO_2$ concentration yields higher sensitivity. Besides this linear trend, no viable relations between sensitivity and gas concentration can be observed; response values are roughly the same, regardless on gas concentration.

Compared to the response against $CO_2$ exposure, exposure to CO yields negligible low responses, ranging from around 2 % at 300 °C (Figure 38) and 350 °C (Figure 39) up to roughly 4 % at 400 °C operating temperature (Figure 40). This directly leads to the assumption that $T_M$ for CO sensing lies above 400 °C for the investigated CuO sensor. This in turn makes the CuO sensor selective for a specific gas, namely $CO_2$, at 300 °C and allows differentiation between $CO_2$ and CO.

## 4.4. Summary of Gas Measurement Results

The sensor responses at different operating temperatures and relative humidity levels under exposure to $CO_2$ and CO are summarized in Table 7.

*Table 7: Estimated maximum sensor responses [%] under exposure to $CO_2$ and CO at different operating temperatures (T) and relative humidiy (rH) levels.*

| ***T [°C]*** | ***Maximum sensor response [%] under exposure to gas*** | | | | | |
|---|---|---|---|---|---|---|
| | *25 % rH* | | *50 % rH* | | *75 % rH* | |
| | *$CO_2$* | *CO* | *$CO_2$* | *CO* | *$CO_2$* | *CO* |
| ***300*** | 10 - 11 | < 2 | 12 | < 2 | 10 | < 2 |
| ***350*** | 7 – 8 | 2 | 8 | < 2 | 6 | < 1 |
| ***400*** | 7 - 6 | 4 - 5 | 5 | 4 | 3 - 4 | 2 - 3 |

The following conclusions can be drawn from the CuO gas sensor evaluation for the exposure to $CO_2$ and CO:

- The sensor shows increased sensitivity to $CO_2$, but low sensitivity to CO,
- The sensor is able to detect low and high $CO_2$ gas concentrations in an alternating mode, which demonstrates the repeatability of the sensor performance,
- The sensor response is influenced by operating temperature and relative humidity,
- Sensitivity to $CO_2$ is highest at an operating temperature of 300 °C and decreases at higher temperatures,
- With a few exceptions, sensitivity to $CO_2$ is highest at relative humidity levels of 25 % and 50 %,
- The response of the gas sensor to $CO_2$ tends to saturate for higher $CO_2$ concentrations.

# 5. Conclusion and Outlook

Within this work, $CO_2$ sensible gas sensors, based on CuO as sensitive material, were successfully fabricated. The CuO thin films were deposited with three different precursor solutions, namely $CuNit_2$, $CuCl_2$ and $CuAc_2$ in different concentrations (0.05, 0.1, 0.2 and 0.3 M), via spray pyrolysis. The optimal spray pyrolysis set up parameters for deposition of CuO thin films were investigated experimentally and are summarized in Table 8.

*Table 8: Optimal set up parameters for CuO deposition via spray pyrolysis.*

| **Parameters** | |
|---|---|
| **Spray time** | 10 min |
| **Precursor solution** | 0.3 M $CuAc_2$ in $H_2O$ |
| **Substrate temperature** | 400 °C |
| **Horizontal sample to nozzle distance** | 33 cm |
| **Vertical sample to nozzle distance** | 6 cm |
| $p_{N2,\ flask}$ | 1.0 bar |
| $p_{N2,\ atomization}$ | 0.3 bar |
| $p_{compressed\ air}$ | 1.1 bar |

Element analysis showed that the chemical composition of the deposited CuO thin films is independent from the used precursor solution and their concentration. All films consist of CuO (tenorite) single phase; no $Cu_2O$ formation has been observed.

Surface analysis revealed thin films fabricated with 0.1 M $CuAc_2$ precursor solution as fine, granular, dense films with an average film thickness of 25 ± 5 nm at a spray time of 10 min. Compared to films deposited with other precursor solutions, $CuAc_2$ yielded the most desirable surface features in terms of homogeneity and roughness.

Regarding film patterning, chemical wet etching with 6 M HCl for 5 – 7 min depending on film thickness is suggested. Argon ion etching instead is unsuitable for etching of CuO thin films.

The fabricated sensor exhibits increased sensitivity to $CO_2$, but only low sensitivity to CO. At 300 °C, the highest responses to $CO_2$ (up to roughly 12 %) were accomplished. Moreover, the sensor response to $CO_2$ decreases with increasing temperature and increasing relative humidity.

The next steps in CuO sensor research, will be proofing the reproducibility of the investigated gas measurements. Moreover, the sensitivity of CuO sensors could be further increased by adding metallic or bimetallic nanoparticles to the thin film's surface. This would increase the sensitive material's surface allowing higher responses to gases. The spray pyrolysis technology for deposition of CuO thin films, which has been developed within this thesis, is suitable for integrating these layers on CMOS-based devices.

# List of Abbreviations

| | |
|---|---|
| AFM | Atomic Force Microscopy |
| AIT | Austrian Institute of Technology |
| CMOS | Complementary Metal Oxide Semiconductor |
| $CuAc_2$ | Copper Acetate Precursor Solution |
| $CuCl_2$ | Copper Chloride Precursor Solution |
| $CuNit_2$ | Copper Nitrate Precursor Solution |
| CuO | Cupric Oxide |
| $Cu_2O$ | Cuprous Oxide |
| CVD | Chemical Vapor Deposition |
| M | mol/litre |
| MCL | Materials Center Leoben |
| MOS | Metal Oxide Semiconductor |
| MUL | Montanuniversität Leoben |
| rH | Relative Humidity |
| SEM | Secondary Electron Microscopy |
| $SnO_2$ | Tin Dioxide |
| $T_M$ | Operating Temperature with Maximum Sensitivity |
| XRD | X-ray Diffration |
| ZnO | Zinc Oxide |

# References


[1] S. Sharma and M. Madou, "A new approach to gas sensing with nanotechnology," *Philosophical transactions. Series A, Mathematical, physical, and engineering sciences*, vol. 370, no. 1967, pp. 2448–2473, 2012.

[2] E. Lackner, *Optimization of CMOS integrated tin oxide gas sensors using metallic and bimetallic nanoparticles,* PhD thesis, Technische Universität Graz, 2017.

[3] G. Eranna, B. C. Joshi, D. P. Runthala et al., "Oxide Materials for Development of Integrated Gas Sensors—A Comprehensive Review," *Critical Reviews in Solid State and Materials Sciences*, vol. 29, 3-4, pp. 111–188, 2010.

[4] Y. Deng, *Semiconducting Metal Oxides for Gas Sensing*, Springer Nature Singapore, 2019.

[5] N. Barsan, D. Koziej, and U. Weimar, "Metal oxide-based gas sensor research: How to?," *Sensors and Actuators B: Chemical*, vol. 121, no. 1, pp. 18–35, 2007.

[6] Marman et al., *Fire and smoke detection and control system*, 1999.

[7] N. Yamazoe, "Toward innovations of gas sensor technology," *Sensors and Actuators B: Chemical*, vol. 108, 1-2, pp. 2–14, 2005.

[8] J. Krainer, *Fabrication of CMOS Integrated Gas Sensor Devices Based on Tungsten Oxide Nanowires,* PhD Thesis, Technische Universität Graz, 2017.

[9] K.-H. Kim, S. A. Jahan, and E. Kabir, "A review of breath analysis for diagnosis of human health," *Trends in Analytical Chemistry*, vol. 33, pp. 1–8, 2012.

[10] G. F. Fine, L. M. Cavanagh, A. Afonja et al., "Metal oxide semi-conductor gas sensors in environmental monitoring," *Sensors*, vol. 10, pp. 5469–5502, 2010.

[11] Wikipedia contributors, "Band gap," 8/5/2019UTC, https://en.wikipedia.org/w/index.php?title=Band_gap&oldid=909442524.

[12] H. Plank, *Microelectronics and Micromechanics*, Technische Universität Graz, 2018.

[13] H.-J. Kim and J.-H. Lee, "Highly sensitive and selective gas sensors using p-type oxide semiconductors: Overview," *Sensors and Actuators B: Chemical*, vol. 192, pp. 607–627, 2014.

[14] R. Schmidt, A. M. F. Benial, and D. D. Anita, *Advanced Environmental Analysis: Applications of Nanomaterials Volume 2*, Royal Society of Chemistry, 2016.

[15] John Vetelino and Aravind Reghu, *Introduction to Sensors*, CRC Press, 2011.

[16] N. Barsan and U. Weimar, "Understanding the fundamental principles of metal oxide based gas sensors: the example of CO sensing with SnO2 sensors in the presence of humidity," *Journal of Physics: Condensed Matter*, vol. 15, pp. 813–840, 2003.

[17] A. Dey, "Semiconductor metal oxide gas sensors: A review," *Materials Science and Engineering: B*, vol. 229, pp. 206–217, 2018.

[18] A. Gurlo, "Insights into the Mechanism of Gas Sensor Operation," in *Metal Oxide Nanomaterials for Chemical Sensors*.

[19] D. E. Williams, “Semiconducting oxides as gas-sensitive resistors,” *Sensors and Actuators B*, vol. 57, pp. 1–16, 1999.

[20] D. Perednis and L. Gauckler, “Thin Film Deposition Using Spray Pyrolysis,” *Journal of Electroceramics*, vol. 14, pp. 103–111, 2005.

[21] J. C. Viguié and J. Spitz, “Chemical Vapor Deposition at Low Temperatures,” *J. Electrochem. Soc. Solid-State Science and Technology*, vol. 122, no. 4, pp. 585–588, 1975.

[22] K. R. Nemade and S. A. Waghuley, “Optical and Gas Sensing Properties of Cuo Nanoparticles Grown by Spray Pyrolysis of Cupric Nitrate Solution,” *International Journal of Materials Science and Engineering*, 2014.

[23] D. Gopalakrishna, K. Vijayalakshmi, and C. Ravidhas, “Effect of annealing on the properties of nanostructured CuO thin films for enhanced ethanol sensitivity,” *Ceramics International*, vol. 39, no. 7, pp. 7685–7691, 2013.

[24] W. DeSisto, M. Sosnowski, F. Smith et al., “Preparation and characterization of copper(II) oxide thin films grown by a novel spray pyrolysis method (1989),” *Materials Research Bulletin*, vol. 24, no. 6, pp. 753–760, 1989.

[25] Wikipedia contributors, “Surface tension,” 7/16/2019UTC, https://en.wikipedia.org/w/index.php?title=Surface_tension&oldid=906588220.

[26] J. Chrzanowski and J. C. Irwin, “Raman Scattering from Cupric Oxide,” *Solid State Communications*, vol. 70, no. 1, pp. 11–14, 1989.

[27] S. Chaurasiya, J. Udaya Bhanu, and P. Thangadurai, “Precursor Dependent Structural Phase Evolution in Hydrothermally Prepared Cu2O Octahedrons and Cu Micro-Flakes and Their Structural and Optical Properties,” *Trans Indian Inst Met*, vol. 71, no. 5, pp. 1185–1191, 2018.

[28] A. Rydosz and A. Szkudlarek, “Gas-Sensing Performance of M-Doped CuO-Based Thin Films Working at Different Temperatures upon Exposure to Propane,” *Sensors (Basel, Switzerland)*, vol. 15, no. 8, pp. 20069–20085, 2015.

[29] N. B. Tanvir, O. Yurchenko, E. Laubender et al., “Zinc peroxide combustion promoter in preparation of CuO layers for conductometric CO2 sensing,” *Sensors and Actuators B: Chemical*, vol. 257, pp. 1027–1034, 2018.

[30] S. Ahlers, G. Müller, and T. Doll, “A rate equation approach to the gas sensitivity of thin film metal oxide materials,” *Sensors and Actuators B: Chemical*, vol. 107, no. 2, pp. 587–599, 2005.

[31] N. B. Tanvir, O. Yurchenko, and G. Urban, “Optimization Study for Work Function Based CO2 Sensing Using CuO-nanoparticles in Respect to Humidity and Temperature,” *Procedia Engineering*, vol. 120, pp. 667–670, 2015.

# List of Figures

# List of Tables